iScience

CellPress
OPEN ACCESS

Article

SARS-CoV-2 variants induce distinct disease and impact in the bone marrow and thymus of mice

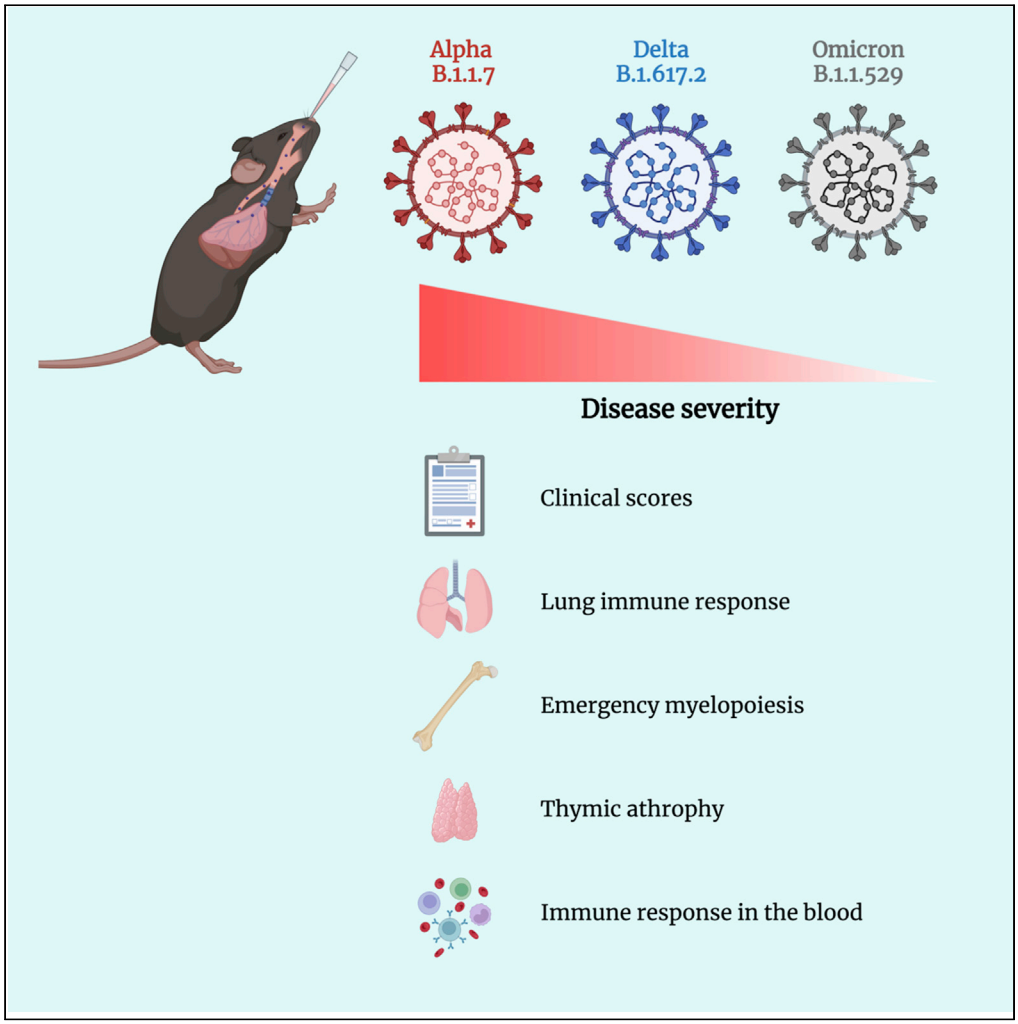

Rute Gonçalves, Joana Couto, Pedro Ferreirinha, ..., Nuno L. Alves, Sofia Lamas, Margarida Saraiva

margarida.saraiva@ibmc.up.pt

Highlights

SARS-CoV2 variants alpha, delta, and omicron induce distinct disease in mice

These variants trigger discrete immune responses, correlating with severity

Infections with variants alpha and delta promote bone marrow emergency myelopoiesis

Infections with the alpha variant lead to marked thymic atrophy

Gonçalves et al., iScience 26, 105972
February 17, 2023
https://doi.org/10.1016/j.isci.2023.105972

iScience

CellPress
OPEN ACCESS

Article

SARS-CoV-2 variants induce distinct disease and impact in the bone marrow and thymus of mice

Rute Gonçalves,[1,6] Joana Couto,[1,6] Pedro Ferreirinha,[1,2] José Maria Costa,[1,3] Diogo Silvério,[1,4] Marta L. Silva,[1,4] Ana Isabel Fernandes,[1,4] Pedro Madureira,[1,5] Nuno L. Alves,[1,2] Sofia Lamas,[1,2] and Margarida Saraiva[1,2,7,*]

SUMMARY

Severe acute respiratory syndrome coronavirus 2 (SARS-CoV-2) has evolved to variants associated with milder disease. We employed the k18-hACE2 mouse model to study how differences in the course of infection by SARS-CoV-2 variants alpha, delta, and omicron relate to tissue pathology and the immune response triggered. We documented a variant-specific pattern of infection severity, inducing discrete lung and blood immune responses and differentially impacting primary lymphoid organs. Infections with variants alpha and delta promoted bone marrow (BM) emergency myelopoiesis, with blood and lung neutrophilia. The defects in the BM hematopoietic compartment extended to the thymus, with the infection by the alpha variant provoking a marked thymic atrophy. Importantly, the changes in the immune responses correlated with the severity of infection. Our study provides a comprehensive platform to investigate the modulation of disease by SARS-CoV-2 variants and underscores the impact of this infection on the function of primary lymphoid organs.

INTRODUCTION

The severe acute respiratory syndrome coronavirus 2 (SARS-CoV-2) infection, which causes the coronavirus disease 2019 (COVID-19), rapidly evolved into a world pandemic. As of June 2022, more than 535 million COVID-19 cases and over 6.3 million deaths were reported (https://ourworldindata.org/). New variants of SARS-CoV-2 have been identified, some of which with increased ability to spread and displace local variants, and/or to evade previously established protective immunological memory responses.[1,2] This has been the case of variants B.1.1.7 (alpha), B.1.617.2 (delta) and most recently B.1.1.529 (omicron), all classified as variants of concern (VOCs) by the WHO and responsible for worldwide COVID-19 waves.[3]

The mouse, owing to its tractability, is an attractive model to study the dynamics of SARS-CoV-2 viral replication, disease pathogenesis, and host immune responses, as well as being used to test therapies and vaccines against COVID-19. Different strategies were developed to overcome the specificity of human versus mouse ACE2 receptor,[4] and thus ensure an efficient SARS-CoV-2 infection. These include the transient delivery of hACE2 by adenoviruses or adenoviral-based vectors,[5] the expression of hACE2 by the mouse promoter[6,7] or as a transgene driven by heterologous gene promoters, as the epithelial cytokeratin-18 (k18) promoter.[8] The k18-hACE2 mouse is widely used in COVID-19 research. Several studies[9–15] show that the intranasal infection of k18-hACE2 mice with SARS-CoV-2 mimics clinical traits of severe infection reported in humans.[16] These include marked lung inflammation, tissue pathology, and impaired function; dissemination of the virus from the lung to other organs; severe neurologic signs and multiorgan failure; pronounced weight loss and limited survival of the animals. Importantly, several studies reported variant-specific effects on the pathogenic patterns and clinical outcomes of SARS-CoV-2-infected k18-hACE2 mice. Both the alpha and beta variants were more lethal than the original SARS-CoV-2 variant.[12] Global differences in survival of k18-hACE2 mice were also reported upon infection with SARS-CoV-2 variants gamma, alpha, beta, iota, and delta.[17] Very recent reports provide evidence for attenuated pathogenicity of the omicron VOC.[18,19] Supported by epidemiologic data available for humans,[1,9,19–22] these studies collectively suggest that intrinsic properties of the viral variant may modulate the course of infection and spectrum of disease.

Despite our growing knowledge of the impact of SARS-CoV-2 infection on the hematopoietic system and how it in turn shapes the outcome of COVID-19, very little is known about the effects of the infection in

[1]i3S - Instituto de Investigação e Inovação em Saúde, Universidade do Porto, 4200-135 Porto, Portugal

[2]IBMC—Instituto de Biologia Molecular e Celular, Universidade do Porto, 4200-135 Porto, Portugal

[3]FEUP—Faculdade de Engenharia, Universidade do Porto, 4200-465 Porto, Portugal

[4]ICBAS—Instituto de Ciências Biomédicas Abel Salazar, Universidade do Porto, 4050-313 Porto, Portugal

[5]Immunethep, Biocant Park, 3060-197 Cantanhede, Portugal

[6]These authors contributed equally

[7]Lead contact

*Correspondence: margarida.saraiva@ibmc.up.pt

https://doi.org/10.1016/j.isci.2023.105972

primary lymphoid organs. Patients with COVID-19 present expansion of neutrophils in the blood and increased recruitment of these cells to the lung,[23,24] with declines in the proportion of circulatory monocytes and an overall severe lymphopenia.[23] Furthermore, an increased abundance of $CD71^+$ erythroid precursors/progenitors was observed in patients with COVID-19,[25] as were episodes of thrombocytopenia and thrombosis.[26] These findings suggest that SARS-CoV-2 infection expectedly impacts in the hematopoietic process, as it has been described for other pathogens. Several pathogens are known to infect the bone marrow (BM) and thymus which, in turn, alter the hematopoietic function of these organs during infection.[27,28]

Here, we compared the infection and pathogenic pattern of the three most recent and high-impact SARS-CoV-2 variants (alpha, B.1.1.7; delta, B.1.617.2; and omicron, BA.1.18/B.1.1.529.1.18) in k18-hACE2 mice. In line with reports in human patients,[1,9,19–22] we found the omicron variant to be the least pathogenic across all different parameters, including clinical scores, organ pathology, and the magnitude of the anti-viral immune response. We also found that infection-induced alterations extended to primary lymphoid organs. Namely, we show that the BM hematopoietic progenitor compartment is altered by the infection, with progenitor cells displaying a bias toward myeloid differentiation, an alteration that may underlie the pronounced neutrophilia seen upon infection with SARS-CoV-2 variants alpha and delta. The thymus was also markedly affected by infection with these variants, showing a severe decrease in its function. The impact of the infection on the tissue, blood, and primary lymphoid organs' immune composition correlated with the severity of infection reflected in the clinical score attributed to each animal. These findings reveal both links between immunity and COVID-19 severity and a broad impact of SARS-CoV-2 infection in primary lymphoid organs, offering exciting avenues for future research toward the understanding of the full impact of SARS-CoV-2 infection in the immune system.

RESULTS

Differential disease outcomes in k18-hACE2 mice infected with SARS-CoV-2 alpha, delta, and omicron variants

To study the relationship between the dose of infection and relative pathogenicity of the SARS-CoV-2 VOCs alpha (B.1.1.7), delta (B.1.617.2), and omicron (B.1.1.529.1.18) in k18-hACE2 mice, we started by comparing the outcome of infection with increasing doses of the alpha variant, given the wealth of available data for this VOC.[12,14,19,29] In line with previous results, infection with the SARS-CoV-2 alpha variant was highly severe across the three tested doses, with poor survival of mice infected with the highest tested dose (1×10^5 PFU) of virus (Figure S1A). Independently of the dose, all infected mice displayed weight loss (Figure S1B) and increased clinical scores (Figure S1C; and Table 1 for clinical scoring criteria) from day 4 post-infection, which despite some variation within each experimental group, correlated with the infectious dose. All animals infected with the high dose displayed neurologic symptoms and over 50% also showed dyspnoea, whereas these symptoms were lower for the other two doses tested (Figure S1D). The macroscopic scoring of several organs was consistent with these findings, with more pronounced alterations seen as the dose of inoculum increased (Figures S1E; and S2A and Table 2 for scoring criteria). Considering the previously described neurologic alterations,[11,30] we analyzed the brain during the necropsy of mice infected with intermediate doses of the alpha variant. Macroscopic scores compatible with brain invasion and damage were attributed to all mice (Figure S1F). Overall, the low and intermediate infection doses of the alpha variant resulted in clinical scores lower than 15 (the adopted value for humane end-point (HEP) application). Clinical and organ scores were directly related, mainly due to graded changes in weight and respiratory distress. Of note, the viral loads assessed by RNA quantification in the lungs on day 6 post-infection were significantly higher in the case of the high infection dose (Figure S1G).

Given the extreme severity observed for the intermediate and highest viral doses, we infected k18-hACE2 mice with the lowest tested dose (1×10^4 PFU) of SARS-CoV-2 delta (B.1.617.2) or omicron (B1.1.529.1.18) variants and compared the course of infection to that of a similar dose of the alpha variant, over 6 days. Lowest clinical scores were observed for mice infected with the omicron variant, followed by alpha- and delta-infected mice (Figure 1A; and Table 1 for clinical scoring criteria). None of the animals infected with the omicron variant reached the clinical score for HEP (Figure 1A). The three variants commonly led to weight loss, which was aggravated in infections with alpha and delta variants (Figure 1B). Overall, mice infected with the alpha variant displayed the highest diversity of symptomatology, with 100% of them exhibiting piloerection and behavioral changes (Figure 1C), whereas 100% of mice infected with a

Table 1. Clinical score sheet for general SARS-CoV-2 infection

Parameter		Score
Body weight	No changes	0
	1–6% loss	1
	7–14% loss	2
	15–19% loss	3
	20–24% loss	4
	>25% loss	HEP
Body condition score[a]	BCS normal (2–3)	0
	Low BCS (1–1,5)	1
Appearance	Normal	0
	General lack of grooming or piloerection	1
	Ocular/Nasal discharge	2
	Eyes closed	3
Behavior	Normal	0
	Minor changes or exaggerated response when provoked	1
	Less mobile/isolated but alert	2
	Restless or still, not alert	3
Neurological	No alterations	0
	Tremor	2
	Ataxia	2
	Seizures	HEP
Hydration	Normal	0
	Abnormal skin test pinch	3
Respiratory movements	Normal	0
	Increased/decreased respiratory frequency	3
	Severe dyspnoea (gasping)	HEP
Total score		(sum)

[a]BCS classification according to.[31] Alterations to BCS were uncommon independent of the variant, as this work involves an acute infection; BCS should, however, be used for chronic infection.

delta variant displayed dyspnoea (Figure 1C). Macroscopic inspection of the lung on day 6 post-infection showed that all mice infected with the delta variant displayed alterations, including hemorrhagic, edematous, or congestive areas, whereas lung macroscopic alterations upon infection with the alpha and the omicron variants were variable (Figure 1D; and Figure S2A and Table 2 for scoring criteria). Furthermore, we detected macroscopic alterations in the stomach and intestine of mice infected with alpha or delta variants, including hemorrhagic stomach and diarrheic or gaseous intestine, but not in omicron-infected counterparts (Figures 1E; and S2A and Table 2 for scoring criteria). Surprisingly, we also noted severe macroscopic alterations to the thymi of k18-hACE2 mice upon infection with the alpha or the delta variants (Figures 1F; and S2A and Table 2 for scoring criteria). No macroscopic alterations were noticed in other analyzed organs, including the heart, bladder, liver, spleen, and kidney.

The original Wuhan and the alpha variants have been described to promote severe alterations to the brain of infected mice, accompanied by virus replication,[9–15,17,30,32] but less is known regarding the pattern of brain invasion during the infection of k18-hACE2 mice with the delta and omicron variants. As compared to non-infected controls (Figure S2B), histologic alterations, such as small infiltrates of inflammatory cells, cellular debris, and hemorrhage, were found in the brains of mice infected with SARS-CoV-2 delta variant, but not with the omicron one (Figure 1G). No visible alterations to the cerebellum were noted. Although the presence of viral nucleocapsid was detected in both cases, it was much more pronounced in delta-infected mice which showed extensive virus-positive detected areas (Figures 1H and S2C for non-infected control).

Table 2. Organ scoring criteria for macroscopic alterations

Score	Lung	Digestive System	Thymus	Brain
0	Normal	Normal	Normal	Normal
1	Collapsed Edematous Congestive Necrotic	Diarrheic or Gaseous	Congested, Edematous or Necrotic	Focal hemorrhagic
2	Hemorrhagic	Hemorrhagic	Hemorrhagic	Multifocal hemorrhagic

These data suggest that the infection of k18-hACE2 with the SARS-CoV-2 alpha variant induced pathology in different organs and thus presented the widest symptoms. The delta variant mainly affected the respiratory outcome and the omicron variant was the least severe of the three. Overall, these differential outcomes of infection mimic the clinical manifestations reported in humans.[1,9,19–22]

Lung pathology and immune responses induced by SARS-CoV-2 variants

To investigate the effects of infection with each SARS-CoV-2 variant on the respiratory tract, we analyzed the histologic alterations and viral content in the lungs of infected k18-hACE2 mice. Lung lesions composed of immune infiltrates, mostly lymphocytes, macrophages and neutrophils, distributed in perivascular and peribronchiolar locations, as well as interstitial congestion and epithelial changes (thickened epithelium) were visible 6 days post-infection, mainly in delta- and omicron-infected lungs (Figures 2A; and S2D for non-infected controls). Of note, more extensive and dispersed lesions were observed in k18-hACE2 mice infected with the delta variant (Figure 2A). Quantification of the lesion area and histopathology scoring (see Table 3 for scoring criteria) supported a stronger impact of the delta variant in the lung tissue (Figure 2A, right panel). On day 6 post-infection, we only detected viral nucleocapsid staining in delta-infected mice (Figures 2B; and S2E for non-infected controls). However, viral RNA was detected in lungs of all infected mice, to levels that were similar for alpha and delta infections and lower for omicron infections (Figure 2C). This likely reflects the ability of the host to control omicron infection in the lung. Next, we analyzed the nasal turbinates of mice infected with the delta and the omicron variants. Overall, at day 6 post-infection, the nasal cavities of infected mice showed intact olfactory and respiratory epithelia (Figures 2D; and S2F for non-infected controls), with small pathological changes that included areas of hemorrhage, inflammatory infiltrates, cellular debris, and mucus exudate (Figure 2D). Despite the differences found in the detection of the viral nucleocapsid in the lung, a positive signal was observed in the nasal turbinates of mice infected with either variant (Figures 2E; and S2G for non-infected controls).

The expression of genes encoding inflammatory cytokines consistently associated with SARS-CoV-2 infection, such as TNF, type I and II IFN, IL-10, IL-6, and IL-1β, was then measured in the lungs of infected animals on day 6 post-infection. The expression patterns of these cytokines differed according to the infecting viral variant (Figure 2F). In agreement with previous reports,[12,14] infection with the alpha variant at this time point coincided with poor expression of inflammatory mediators in the lungs (Figure 2F). k18-hACE2 mice infected with the delta or omicron variants displayed similar patterns of *tnf*, *il10*, *il6*, and *il1b* gene expression (Figure 2F). Mice infected with the delta variant displayed the highest expression levels of *ifnb*, whereas infection with the omicron variant induced the highest expression of *ifng* and *il17* (Figure 2F). To complement the gene expression analysis, we measured the amount of IFN-γ present in the bronchoalveolar lavage of mice infected with either SARS-CoV2 variant. In line with the transcriptional data, we found lower levels of IFN-γ associated with alpha infections (Figure 2G). However, despite the differences in *ifng* transcripts on day 6 post-infection, the accumulation of this cytokine in the bronchoalveolar lavage of mice infected with delta or omicron variants was similar (Figure 2G).

Lastly, the immune cell composition of lung cell suspensions was analyzed by flow cytometry (see Figure S3A for gating strategy and Figure S3B for non-infected controls). We found a striking difference in the frequency and number of hematopoietic cells ($CD45^+$) in the lungs of alpha-infected mice (Figures 3A and 3B). Furthermore, infection of k18-hACE2 mice with the alpha variant resulted in marked alterations to the lung immune cell composition, namely a decrease in the frequency of $CD11b^+$ cells, monocytes, and recruited macrophages and a massive increase in neutrophils (Figure 3A). The increase in the frequency of neutrophils was also seen in the other two infections, but was not as marked (Figure 3A). Infections with delta or omicron variants resulted in increased frequencies and numbers of monocytes

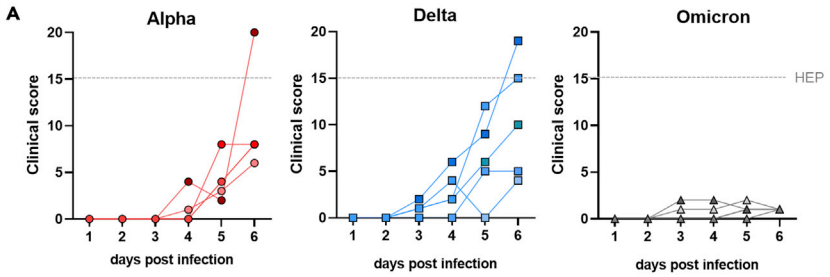

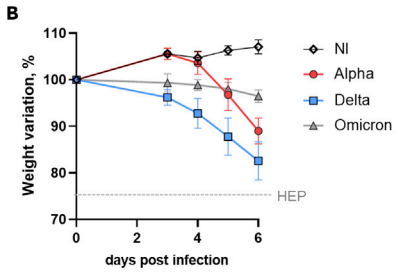

C

	Frequency, %		
Symptoms, day 6	Alpha	Delta	Omicron
Weight loss	100%	100%	80%
Ocular/Nasal discharge	20%	0%	0%
Piloerection	100%	40%	0%
Eyes semi/closed	20%	0%	0%
Dehydration	80%	60%	0%
Behaviour changes/Lethargy	100%	40%	0%
Dyspnea	40%	100%	0%

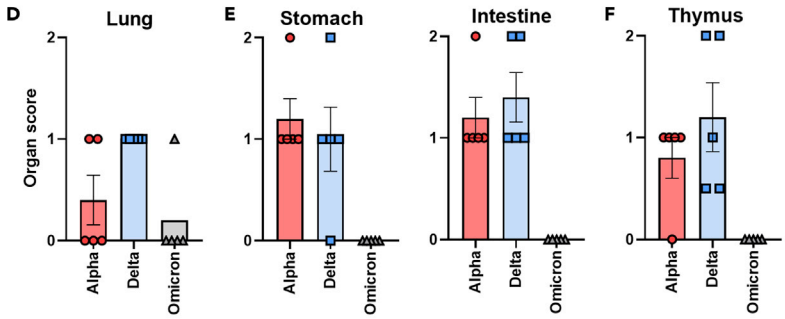

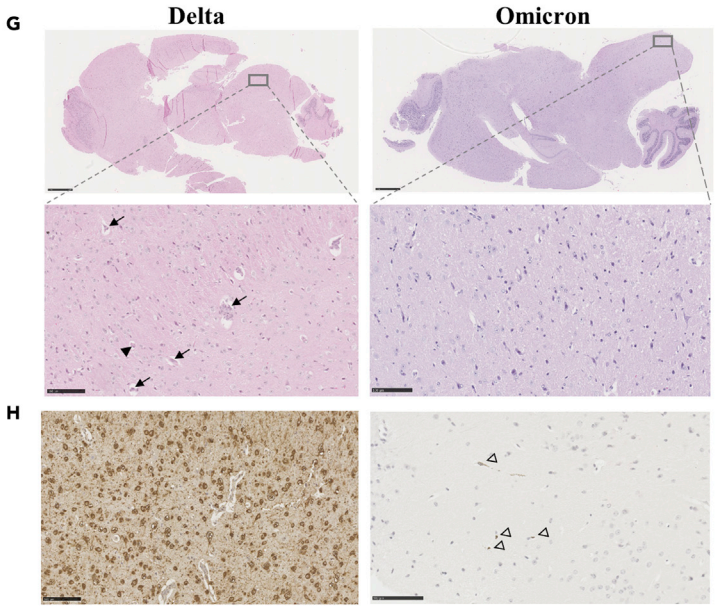

Figure 1. Infection of k18-hACE2 mice with SARS-CoV-2 alpha, delta or omicron variants results in differential disease outcomes

k18-hACE2 mice were intranasally infected with 1 × 10^4 PFU of the indicated SARS-CoV-2 variant.

(A) Clinical score evolution. Each mouse was observed on day 0 and daily from day 3 post-infection and a clinical score attributed. Clinical scores of 15 or above were considered humane endpoints (HEP; dotted lines).

(B) Percentage of weight variation over time. Initial weight on day 0 is considered 100% and from day 3 post-infection the variation calculated for each mouse.

(C) On day 6 post-infection the frequency of mice displaying each indicated symptom across the three infections was registered.

(D–F) During necropsy, a macroscopic inspection of several organs was performed and an organ score reflecting visible alterations attributed.

(G) Representative images of brain tissue slices stained with H&E. Rectangles and dashed lines indicate the region enlarged below. Inflammatory cells (arrowhead) and cellular debris (arrow) are indicated. Scale bars represent 1 mm (upper panels) and 100 μm (lower panels).

(H) Brain tissue slices were stained with a specific antibody against the viral nucleocapsid. Stained areas (brown, open arrowhead) indicate the presence of viral particles in the tissue. Scale bars represent 100 μm. A, D-F. Each symbol represents an individual mouse of a group of five used in each infection. B, D-F. Represented is the Mean ± SEM for each group.

within the $CD11b^+$ subset, with the same happening for recruited macrophages in the case of omicron infections (Figures 3A and 3B). Common to the three infections was the increased frequencies and numbers of $CD11c^+$ DCs on day 6 post-infection (Figures 3A and 3B) and decreased values for alveolar macrophages and eosinophils (Figure S3C). Within the lymphoid branch, we observed a decreased frequency of $CD19^+$ B cells for all variants, a specific decrease in the frequencies and numbers of $CD4^+$ T cells in alpha-infected animals and an increase in the representation of $CD8^+$ T cells in the omicron infection (Figures 3A and 3B). Of note, k18-hACE2 mice infected with the alpha variant displayed low numbers of all immune cell populations in the lungs due to the highly reduced $CD45^+$ cell numbers (Figure 3B). Because several reports support that neutrophilia and lymphopenia act as complementary drivers of severe COVID-19 outcomes,[33–35] we calculated the ratios of neutrophils to T or B cells for the three experimental infections. Only infection of k18-hACE2 mice with the omicron VOC resulted in decreased ratios of neutrophil to $CD4^+$ and $CD8^+$ T cells, or $CD19^+$ B cells (Figure 3C). To gain insight into possible mechanisms underlying the differential lung recruitment of neutrophils versus monocytes/macrophages across the different infections, we measured the expression of *ccl2*, *cxcl9*, and *cxcl2* in mice infected with the different SARS-CoV2 variants. We observed a higher expression of the *ccl2* and *cxcl9* genes, and a lower expression of the *cxcl2* gene, in the case of delta and omicron infections (Figure 3D). Given that CCL2 and CXCL9 attract monocytes/macrophages and CXCL2 neutrophils,[36] the imbalance in their expression may at least in part explain the different immune cell compositions observed.

Infection of k18-hACE2 mice with SARS-CoV-2 variants distinctly alters the circulating immune cell composition

We next questioned whether alterations in immune cell populations could be monitored in the blood from earlier time points post-infection. To answer this, peripheral blood of naive or infected k18-hACE2 animals was analyzed by flow cytometry on days 3 and 6 post-infection (see Figure S3D for gating strategy and Figure S3E for non-infected controls). From day 3 to day 6 post-infection, the frequency of neutrophils was increased in infections with alpha and delta variants, but stable in mice infected with the omicron variant (Figure 4A). Additionally, a decrease in the frequency of monocytes between days 3 and 6 post-infection was only seen for infections with the alpha variant (Figure 4A). On day 6 post-infection, the frequency of $CD11c^+$ DCs was increased in infected animals independently of the viral variant (Figure 4A), but this frequency was only increased on day 3 in the case of omicron-infected mice (Figure 4A). No major changes were detected for $CD19^+$ B cells in infected vs non-infected mice, whereas for both $CD4^+$ and $CD8^+$ T cells a decrease was seen from day 3 to day 6 in mice infected with the alpha variant (Figure 4B). Interestingly, as compared to non-infected controls, mice infected with the delta variant showed a transiently decrease in T cells by day 3 (Figure 4B). No variation in the frequency of these cells was observed in omicron-infected mice (Figure 4B). We also calculated the neutrophil to T or B cells ratio and found that the most pronounced increase of this value corresponded to mice infected with the alpha variant for 6 days (Figure 4C). Together, our results reinforce that neutrophilia is an effective indicator of disease severity in SARS-CoV-2-infected k18-hACE2 mice, as reported in human patients,[37] suggesting that a premature assessment of these parameters in the blood may be a useful biomarker to test early therapeutic interventions for COVID-19.

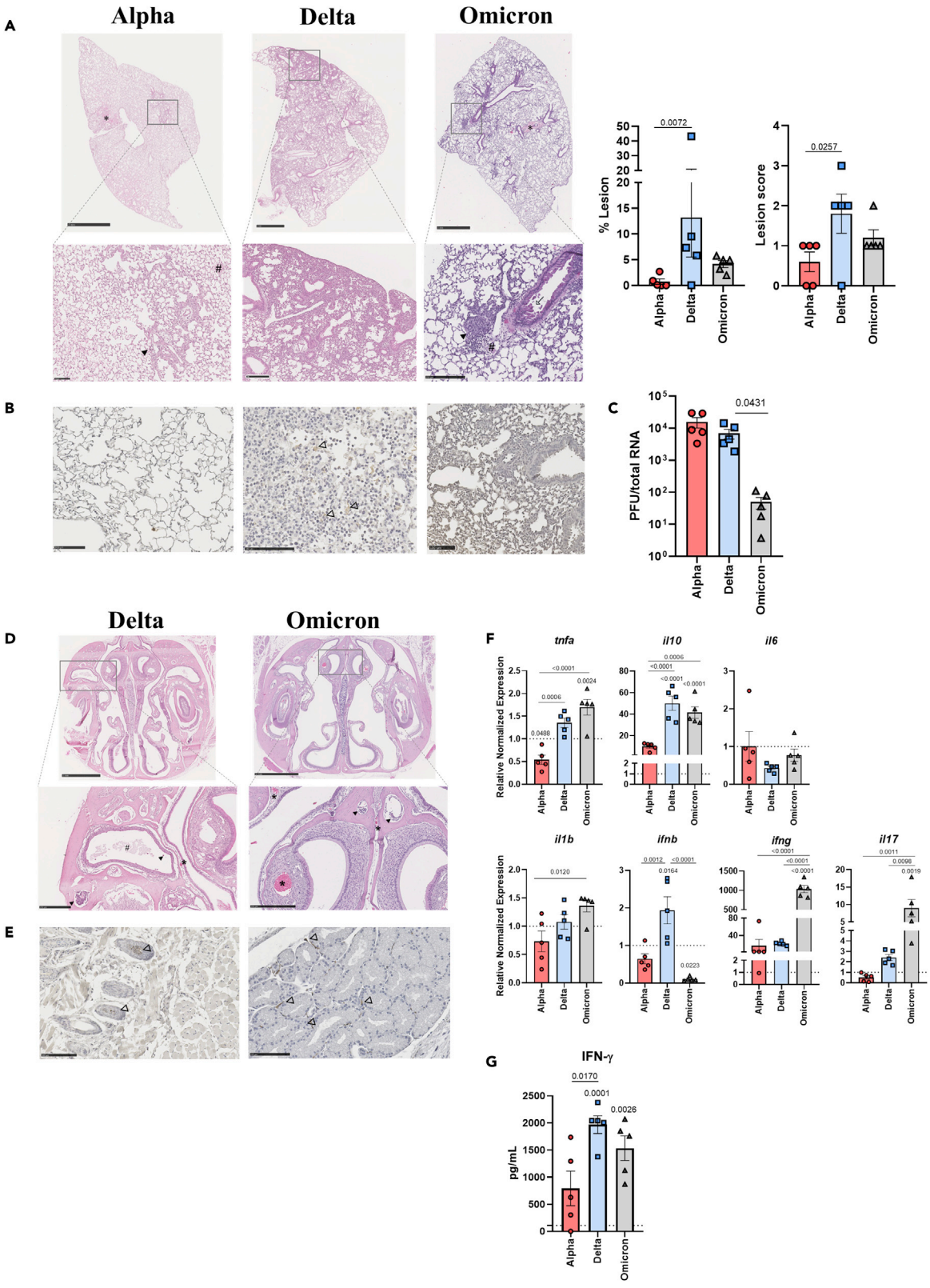
A
Alpha
Delta
Omicron
% Lesion
0.0072
Lesion score
0.0257
B
C
PFU/total RNA
0.0431
D
Delta
Omicron
E
F
tnfa
il10
il6
il1b
ifnb
ifng
il17
Relative Normalized Expression
G
IFN-γ
pg/mL
0.0170
0.0001
0.0026

Figure 2. Impact of SARS-CoV-2 alpha, delta, and omicron variants on the respiratory tract of infected k18-hACE2 mice

k18-hACE2 mice were intranasally infected with 1 × 10^4 PFU of the indicated SARS-CoV-2 variant. On day 6 post-infection mice were humanely euthanized and the lungs and nasal turbinates recovered.

(A and B) Representative images of tissue slices of lungs of infected mice stained with H&E (A) or a specific antibody against the viral nucleocapsid (B). In A, a histopathology score was attributed to H&E stained lungs and the area of lesion automatically calculated.

(C) Virus quantification at day 6 post-infection. Based on the detection of viral RNA and on quantified standard curves, the number of viral particles (PFU) in the lungs of infected mice was calculated. D, E. Representative images of tissue slices of nasal turbinates of infected mice stained with H&E (D) or a specific antibody against the viral nucleocapsid (E).

(A and D) Rectangles and dashed lines indicate the regions enlarged in lower panels. Thickened epithelium (open arrow); inflammatory cell infiltrates (arrowhead); hemorrhage (*) and cellular debris/exudate (#) are indicated.

(B and E) Stained areas (open arrowhead) indicate the presence of viral particles in the tissue. Scale bars represent 1 mm (top panels) and 250 μm (bottom panels), except for the lung image of mice infected with the alpha VOC which is 100 μm.

(F) Relative expression of cytokine genes in the lung of infected animals. mRNA was extracted, the expression of the indicated genes measured by real-time PCR and normalized using *gapdh* and *ubiquitin* reference genes. The expression of non-infected mice is set to 1 (dotted line).

(G) IFN-γ levels detected by immunoassay on day 6 post-infection in the bronchoalveolar lavage of infected mice. A, C, F, G. Represented is the Mean ± SEM for each experimental group and individual mice shown as discrete symbols. Statistical analyses were conducted using the Kruskal-Wallis test (A), Brown-Forsythe and Welch ANOVA test (C), and one-way ANOVA (F, G). Differences between groups were considered significant if $p < 0.05$. *p* values shown above bars refer to differences to non-infected mice.

Severe SARS-CoV-2 infection promotes emergency myelopoiesis in the bone marrow

Given the alterations in the mature hematopoietic compartment of SARS-CoV-2-infected k18-hACE2 mice, which parallel those described in patients with COVID-19,[23] we hypothesized that infection with SARS-CoV-2 may skew the BM function and output. The composition of the hematopoietic progenitor populations in the BM of control or SARS-CoV-2-infected mice was thus analyzed (see Figure S4A for gating strategies and Figure S4B for non-infected controls). Differences in the BM progenitor compartment across the infections with the three viral variants under study were observed, as compared to control mice. Whereas the lineage$^-$Sca-1$^-$c-Kit$^+$ (LK) population was decreased in mice infected with the alpha and the delta variants, this population was increased in the case of the omicron infection (Figure 5A). Moreover, as compared to non-infected mice and within the LK population, a significant decrease in the frequency of common myeloid progenitors (CMPs) was observed for alpha and delta infections, while this population was increased upon omicron infections (Figure 5B). In contrast, the frequency of granulocyte/macrophage progenitors (GMPs) was significantly increased in mice infected with the alpha variant, unchanged in those infected with the delta variant and decreased upon omicron infection (Figure 5B). Finally, no marked alterations were detected for the frequency of megakaryocyte/erythrocyte progenitors (MEPs), with the exception of an increase in omicron-infected mice (Figure 5B). The main difference associated with the less severe omicron infection was thus an inversion of the CMP/GMP proportions when compared to the more severe alpha and delta infections. Infection of k18-hACE2 mice with all variants resulted in an increase in the frequency of lineage$^-$Sca-1$^+$c-Kit$^+$ (LSK) cells, which was more pronounced in the case of the delta and omicron infections (Figure 5C). The frequency of long-term (LT) and short-term (ST) hematopoietic stem cells (HSCs) within LSKs moderately fluctuated during the course of infection without a variant-associated pattern (Figure 5D). In contrast, the frequencies of the myeloid-biased progenitors MPP2 and MPP3 within the LSKs augmented in all three infections (Figure 5D). The frequencies of lymphoid-biased MPP4 and CLPs remained similar in all groups of mice, independently of the infection (Figure 5E). Collectively, these data suggest that the infection of mice with SARS-CoV-2 variants remodels the hematopoietic progenitor compartment in the BM, mainly through an increase in myeloid-biased populations which likely sustains myeloid amplification.

Thymopoietic alterations in SARS-CoV-2-infected k18-hACE2 mice

The atrophic thymus of mice infected with more pathologic variants (Figure 1F) suggested possible alterations in thymic function. Since thymopoiesis requires a continual input of BM progenitors[38] and the

Table 3. Histopathology scoring criteria for lung lesions

Score	Lesion characteristics
0	No lesions
1	Small and localized lesion
2	Multiple small lesions
3	Extensive lesions
+1	Extra point if congestion/edema/epithelium thickening are present

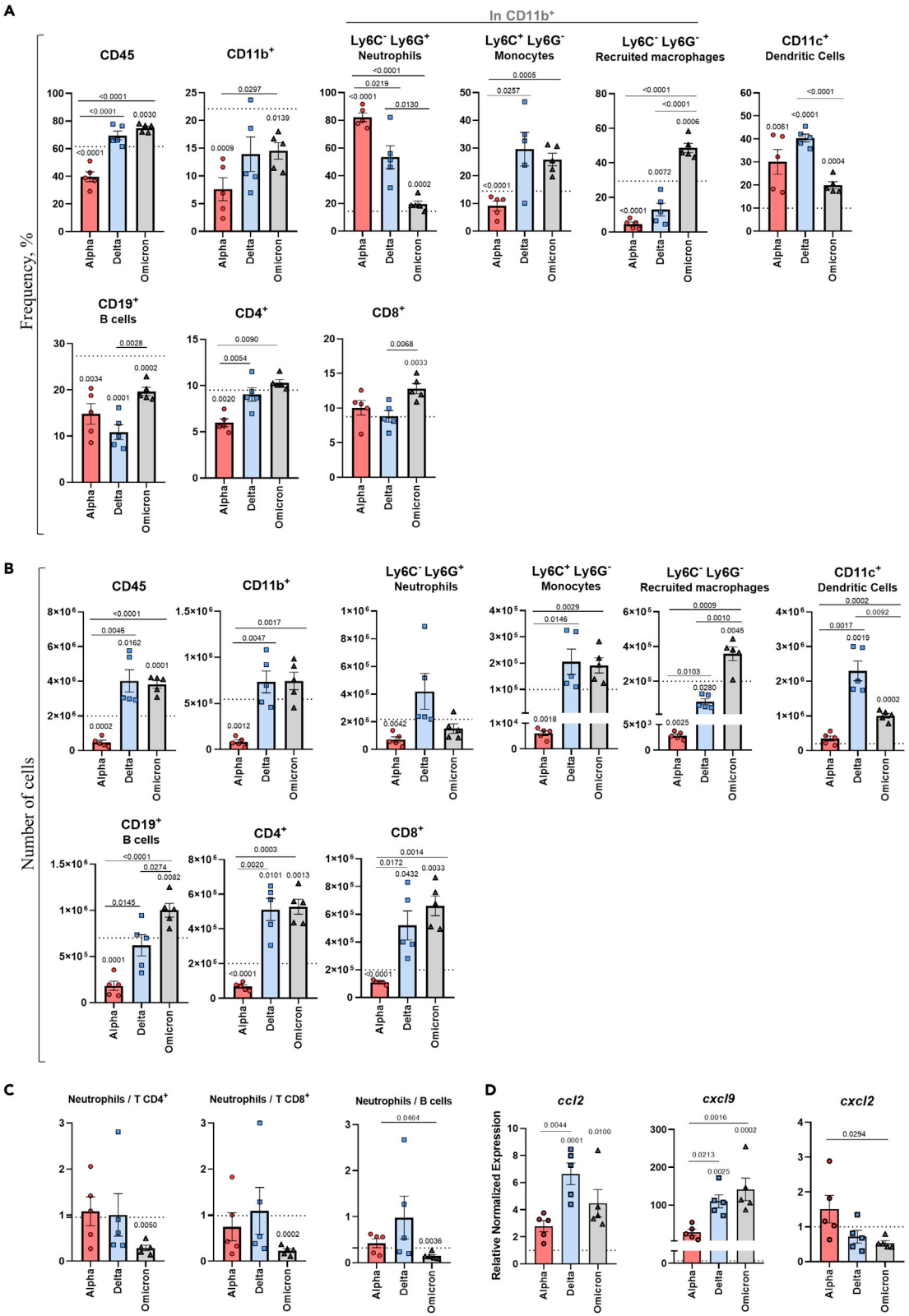
A
In CD11b+
CD45
CD11b+
Ly6C- Ly6G+ Neutrophils
Ly6C+ Ly6G- Monocytes
Ly6C- Ly6G- Recruited macrophages
CD11c+ Dendritic Cells
CD19+ B cells
CD4+
CD8+
Frequency, %
Alpha
Delta
Omicron
B
Number of cells
C
Neutrophils / T CD4+
Neutrophils / T CD8+
Neutrophils / B cells
D
ccl2
cxcl9
cxcl2
Relative Normalized Expression

Figure 3. Distinct immune cell recruitment to the lungs of k18-hACE2 mice infected with SARS-CoV-2 alpha, delta or omicron variants

Lung cell suspensions were prepared from k18-hACE2 mice on day 6 post-infection and the indicated immune cell populations detected by multiparametric flow cytometry. Gating strategies are in Figure S3. Naive k18-hACE2 mice were used as controls.

(A and B) Frequency and B. numbers of the analyzed immune cell populations.

(C) Ratios of neutrophils to $CD4^+$ T, $CD8^+$ T cells, or $CD19^+$ B cells calculated from cell numbers in the total lung.

(D) Relative expression of *ccl2*, *cxcl9* and *cxcl2* genes in the lung of infected animals, day 6 post-infection. mRNA was extracted, the expression of the indicated genes measured by real-time PCR and normalized using *gapdh* and *ubiquitin* reference genes. Represented is the Mean ± SEM for each experimental group and individual mice shown as discrete symbols. The dotted lines in each graph refer to the mean on non-infected mice, and the individual values are represented in Figure S3. Statistical analyses were conducted using the one-way ANOVA e Brown-Forsythe and Welch ANOVA test (A-C) and one-way ANOVA(D). Differences between groups were considered significant if $p < 0.05$. *p* values shown above bars refer to differences to non-infected mice.

composition of hematopoietic precursors in the BM was differentially affected upon infection, we examined how T cell development unfolded under different conditions. The total thymic cellularity was increasingly affected by the infection with omicron, delta, and alpha (Figure 6A). Strikingly, the thymus of delta- and alpha-infected mice presented increasingly alterations in the frequencies of double-negative (DN), double-positive (DP), and single-positive (SP) thymocytes (Figures 6B; and S4C and S4D for non-infected controls). These developmental defects led to a significant reduction in the number of DP and SP4 and SP8 T cells (Figure 6C). Infection of mice with the omicron variant had the least impact on the thymus (Figure 6). Collectively, these data suggest that the capacity of the thymus to maintain normal T cell development is severely compromised in the course of SARS-CoV-2 infections.

Severity of infection correlates with distinct immunological parameters

To gain insight into how the observed alterations to the immune system may relate to disease severity, we searched for correlations between the assessment of the immune status in the tissue (lung), blood, and primary lymphoid organs (BM and thymus) and the clinical score obtained for each mouse across the three infections. The frequency and/or numbers of bulk hematopoietic ($CD45^+$) cells, recruited macrophages, monocytes, $CD19^+$ B, and $CD8^+$ T cells within the lung correlated negatively with the clinical score obtained on day 6 post-infection, whereas the ratios of neutrophils to lymphocytes correlated positively (Figure 7A). In the blood, the ratios neutrophils/T cells also correlated positively with increased severity on day 3 post-infection (Figure 7B), suggesting that these ratios may be of use as proxies to predict the severity of the infection. Alterations in the LK, CMP, and MPP3 compartments in the BM all negatively correlated with the clinical score, whereas those seen in the GMP compartment positively correlated with the severity of infection in k18-hACE2 mice (Figure 7C). Finally, the disruption of the thymus composition markedly correlated with disease severity, with a strong positive correlation established between severe disease and the frequencies of DN, SP4, and SP8 and a negative one with DP cells (Figure 7D). In conclusion, by analyzing the impact of different SARS-CoV-2 variants on the broad immune response, we found immune alterations at the site of infection, blood, BM, and thymus that correlated with the severity of SARS-CoV-2 infection in mice.

DISCUSSION

k18-hACE2 mice are widely used as models for experimental SARS-CoV-2 infection, to test novel therapies and vaccines, but also to deepen our understanding of disease pathogenesis, viral replication, and the host immune responses during infection. Additionally, defining the course of infection in k18-hACE2 mice has been important to reveal intrinsic pathogenic properties of SARS-CoV-2 variants.[12,14,18,19] Our study supports previous reports showing a decrease in the virulence of emerging SARS-CoV-2 variants. In accordance with recent studies in animal models[18,19] and humans,[39] the omicron variant is less pathogenic than the alpha and delta ones, showing minimal clinical, histological, and immunological scores. At the same time, our data reveal distinct features of the immune response developed upon infection with these three variants. Unveiling correlates of protection associated with SARS-CoV-2 omicron infection may contribute to the development of better prognosis and therapeutic tools for COVID-19.

We report a more pronounced impact caused by infections with the delta variant at the main site of infection by SARS-CoV-2, the lung.[40] Our study expands on previous ones[18,19] as immunological analyses of the lung across the tested variants are included. In what concerns cytokine gene expression in the lung on day 6 post-infection, the main specific feature of SARS-CoV-2 omicron infections was the increased expression of *ifng* and *il17* genes. This may contribute to a more competent or prolonged T cell response in these infections, which in turn may lead to better control of the virus. Worth mentioning, a recent report[19] documented low expression of the *ifng* gene in the lung of SARS-CoV-2 omicron infected k18-hACE2 mice,

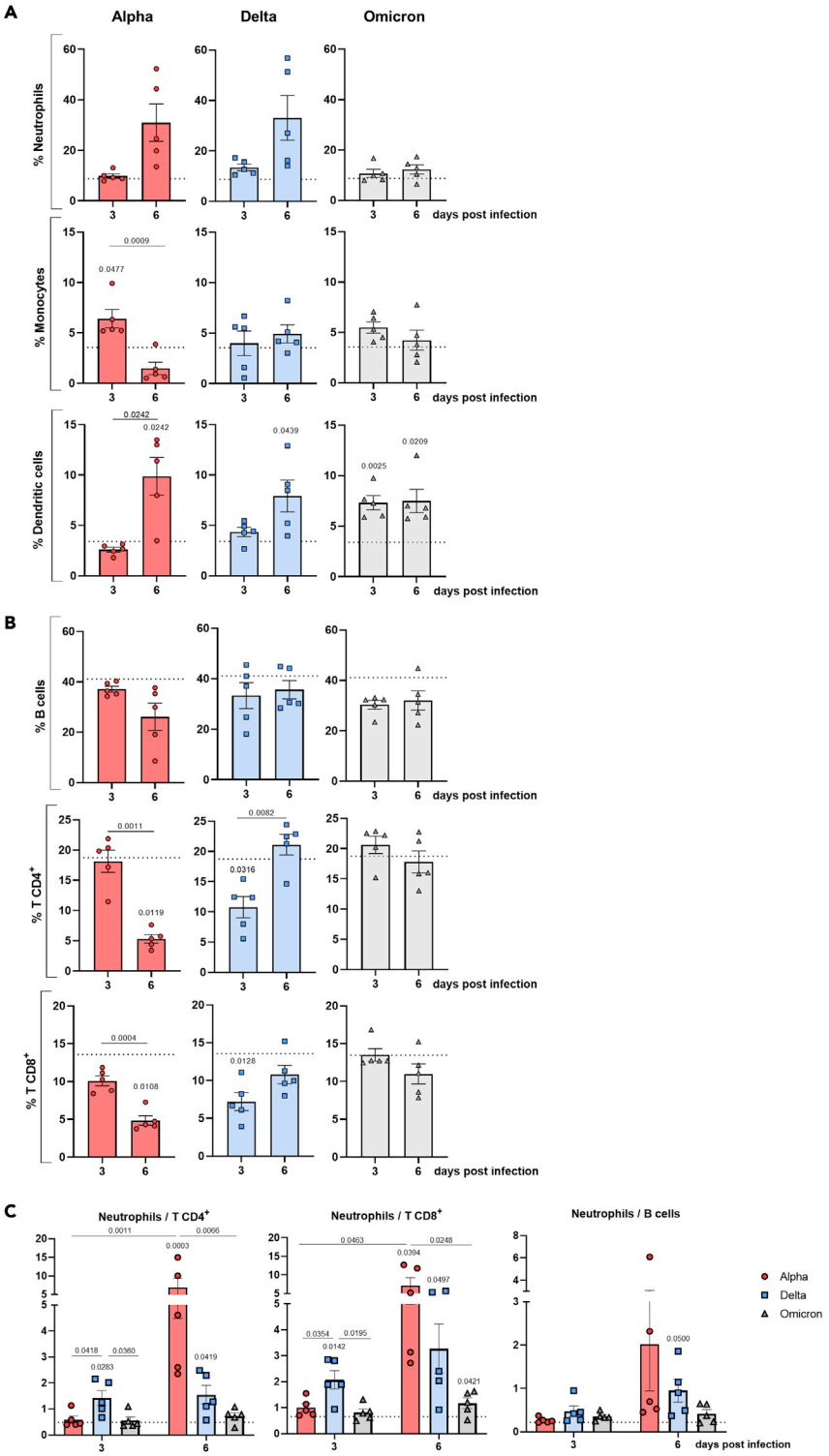

Figure 4. Longitudinal analysis of blood immune cell populations of k18-hACE2 mice infected with SARS-CoV-2 alpha, delta or omicron variants

Blood samples of k18-hACE2 mice were collected on days 3 and 6 post-infection and the indicated immune cell populations detected by multiparametric flow cytometry. Gating strategies are in Figure S3. Naive k18-hACE2 mice were used as controls.

Figure 4. *Continued*

(A and B) Myeloid and B. lymphoid cell frequencies at the indicated time points post-infection with alpha, delta or omicron variants.

(C) Ratios of neutrophils to $CD4^+$ T, $CD8^+$ T or $CD19^+$ B cells calculated from data in A and B. Represented is the Mean ± SEM for each experimental group and individual mice shown as discrete symbols. The dotted lines in each graph refer to the mean on non-infected mice, and the individual values are represented in Figure S3. Unpaired one-way or Brown-Forsythe and Welch ANOVA tests were used to perform comparisons between groups. Differences between groups were considered significant if $p < 0.05$. *p* values shown above bars refer to differences to non-infected mice.

as compared to alpha or delta infections. However, in contrast to our day 6 post-infection analysis, in the previous study the expression of *ifng* was measured on days 2 and 4 post-infection. It is possible that *ifng* gene expression needs to be tightly regulated during the course of infection. While enhanced expression of *ifng* may underlie a detrimental pro-inflammatory response at an early stage of infection, as suggested in patients with severe COVID-19,[41–43] at a later time point it may become beneficial. The fact that the levels of IFN-γ protein were similar in the bronchoalveolar lavage of mice infected with delta or omicron variants, despite the difference in mRNA levels on day 6, supports the hypothesis of differential transcriptional kinetics. In this sense, it will be important to investigate the kinetics of cytokine expression and production during the infection of k18-hACE2 mice with different SARS-CoV-2 variants. As for immune cell recruitment, overall, and at day 6 post-infection, the alpha variant was associated with reduced numbers of hematopoietic cells in the lungs, possibly reflecting the high damage caused by the infection to this organ. Infections with this variant are furthermore associated with a high frequency of neutrophils and low frequency of monocytes within the $CD11b^+$ population, as well as decreased frequencies of $CD4^+$ lymphocytes. Altogether, these features are aligned with those reported in patients with severe COVID-19.[34,35] At the opposite end of the spectrum were infections with the omicron variant, where much more balanced cellular responses were observed. Of particular note were the lower neutrophil/lymphocyte ratios observed in this case. Although our study does not uncover the mechanistic details underlying the differential immune cell recruitment, our findings offer altered chemokine expression in the lungs of mice infected with the different SARS-CoV2 variants as a possible contributor. Taken together, our data associate infections with the omicron variant with the alleviation of the lung immune response. This was also visible in the peripheral blood of k18-hACE2 omicron-infected mice which lacked the pronounced neutrophilia and lymphopenia observed during alpha infections, and that most likely underlie the hyperinflammatory syndrome in COVID-19.[42]

Although we describe a differential effect of SARS-CoV2 variants in the lung immune cell landscape, whereas the infection of immune cells by the different VOCs may vary was not addressed in our study. Infection of human lung macrophages,[44,45] blood monocytes, monocyte-derived macrophages, and DC,[33,44,46–48] and of B and T lymphocytes[47,49] by SARS-CoV2 has been recently described. Despite being abortive, infection of immune cells by SARS-CoV2 was commonly shown to occur independently of ACE2 and to associate with inflammatory responses and cell apoptosis,[33,44–49] which in turn promote disease severity. Thus, it will be of interest to investigate in the future if the impact of each variant on immune cell composition may also depend on the direct infection of the immune cells during the early stages of disease.

Extrapulmonary COVID-19 is also reported in some patients. Among these, neurologic signs, cardiac dysfunction and gastrointestinal tract symptoms are well-known COVID-19 manifestations.[50–52] We report macroscopic alterations in several extrapulmonary locations, and interestingly show that these alterations varied with the infecting viral variant, being consistently lower in the case of the omicron infection. A recent study reported that the aerosol route of infection prevents SARS-CoV-2 neuroinvasion in k18-hACE2 mice, thus decreasing the severity of disease and contributing to a model that better mimics the diverse outcomes of SARS-CoV-2 infection in humans.[53] It will be important to further study the delta and the omicron variants in the aerosol model of infection. Most interestingly, we show an impact of the infection in primary lymphoid organs, the BM, and the thymus. Of note, perturbation of secondary lymphoid organs has been described before, with reported germinal center destruction in fatal COVID-19 cases.[54,55] The main effect observed in the BM that is common to the three tested VOCs was an increase in the frequencies of the myeloid-biased MPP2 and MPP3 progenitor populations. This alteration may underlie the granulocyte amplification seen in k18-hACE2 mice and also described in patients with COVID-19.[56] However, whereas in mice infected with SARS-CoV-2 alpha or delta variants, we also observed an increase in the GMP population, this was not the case for omicron infections. It is possible that granulopoiesis is enhanced during

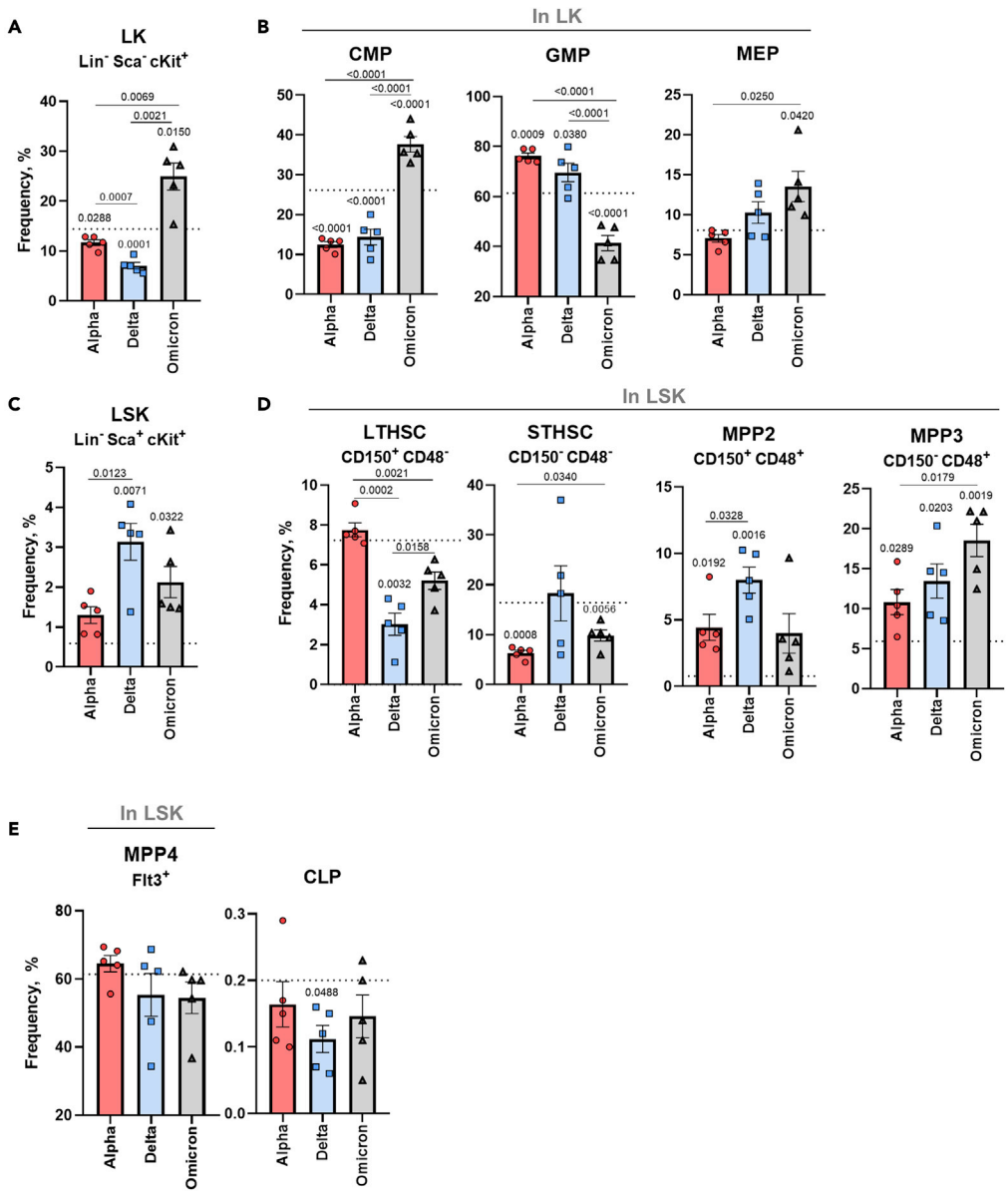

Figure 5. Evidence of emergency myelopoiesis induced by SARS-CoV-2 infection

(A)BM cell suspensions obtained from k18-hACE2 mice on day 6 post-infection were lineage-depleted and stained for hematopoietic progenitor subsets. Gating strategies are in Figure S4. Naive k18-hACE2 mice were used as controls. Frequencies of BM A. LK ($Lin^-IL\text{-}7R\alpha^-cKit^+Sca\text{-}1^-$).

(B) CMP ($Lin^-IL\text{-}7R\alpha^-c\text{-}Kit^+Sca\text{-}1^-FcγRI^{lo}CD34^+$), GMP ($Lin^-IL\text{-}7R\alpha^-c\text{-}Kit^+Sca\text{-}1^-FcγR^+CD34^{hi}$) and MEP ($Lin^-IL\text{-}7R\alpha^-c\text{-}Kit^+Sca\text{-}1^-FcγR^-CD34^{lo}$).

(C) LSK ($Lin^-IL\text{-}7R\alpha^-cKit^+Sca\text{-}1^+$).

(D and E) LT-HSC ($Lin^-IL\text{-}7R\alpha^-c\text{-}Kit^+Sca\text{-}1^+CD150^+CD48^-$), ST-HSC ($Lin^-IL\text{-}7R\alpha^-c\text{-}Kit^+Sca\text{-}1^+CD150^-CD48^-$), MPP2 ($Lin^-IL\text{-}7R\alpha^-c\text{-}Kit^+Sca\text{-}1^+CD150^+CD48^+$) and MPP3 ($Lin^-IL\text{-}7R\alpha^-c\text{-}Kit^+Sca\text{-}1^+CD150^-CD48^+$) and E. MPP4 ($Lin^-IL\text{-}7R\alpha^-c\text{-}Kit^+Sca\text{-}1^+Flt3^+$) and CLP ($Lin^-IL\text{-}7R\alpha^+c\text{-}Kit^+Sca\text{-}1^+$) populations. Represented is the Mean ± SEM for each experimental group and individual mice shown as discrete symbols. The dotted lines in each graph refer to the mean on non-infected mice, and the individual values are represented in Figure S4. Unpaired one-way or Brown-Forsythe and Welch ANOVA tests were used to perform comparisons between groups. Differences between groups were considered significant if $p < 0.05$. *p* values shown above bars refer to differences to non-infected mice.

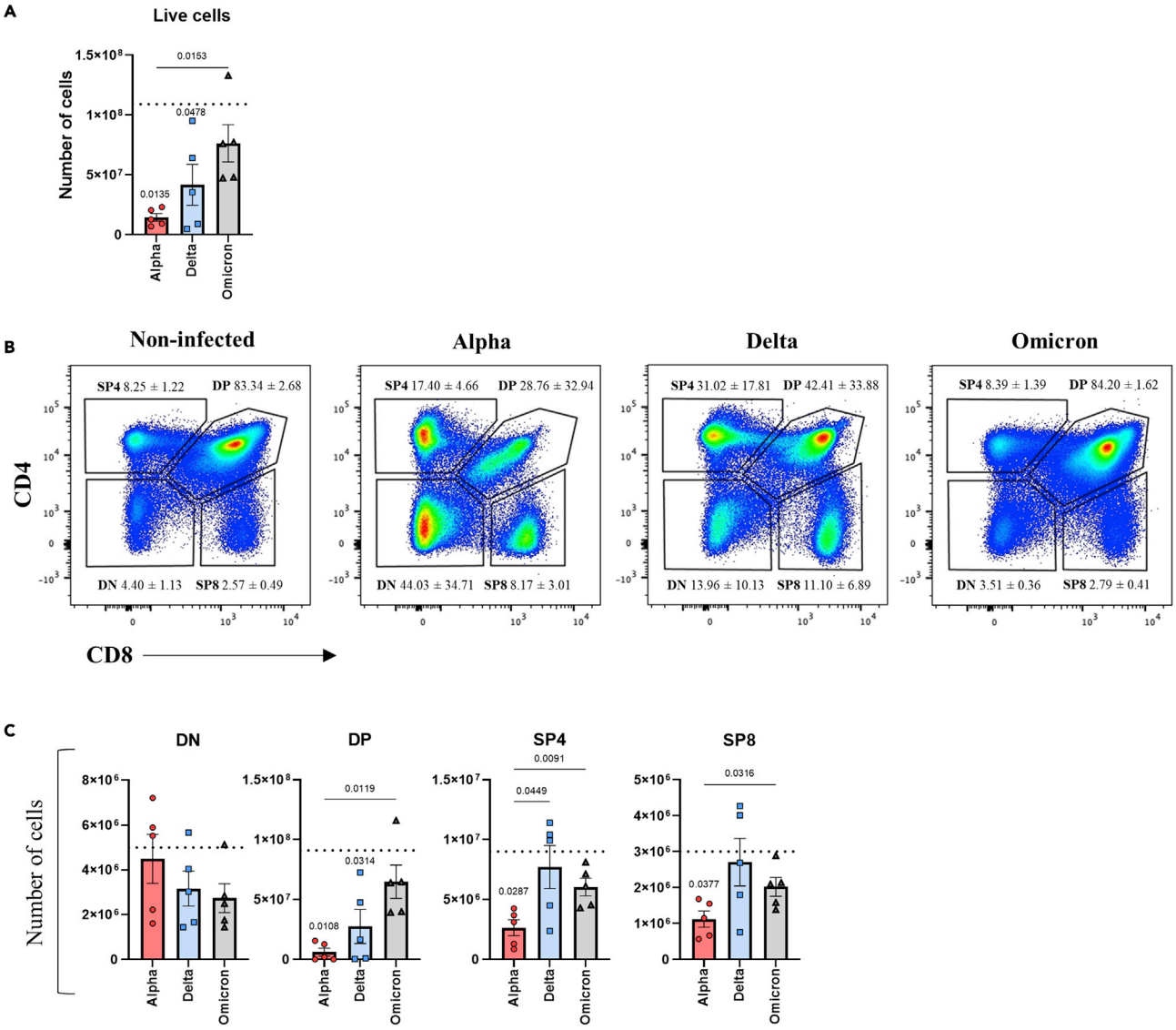

Figure 6. Distinct thymic T cell development during SARS-CoV-2 infections

Thymic cell suspensions obtained from k18-hACE2 mice on day 6 post-infection were stained for thymocyte subsets. Gating strategies are in Figure S4. Naive k18-hACE2 mice were used as controls.

(A) Live cell numbers.

(B and C) Frequency plots and C. numbers of the analyzed thymocyte populations. The maturation stages represented are: double-negative (DN; $TCR^{-}CD4^{-}CD8^{-}$), double-positive (DP; $TCR^{+}CD4^{+}CD8^{+}$), single positive 4 (SP4; $TCR^{+}CD4^{+}CD8^{-}$), and single positive 8 (SP8; $TCR^{+}CD4^{-}CD8^{+}$). Represented is the Mean ± SEM for each experimental group and individual mice shown as discrete symbols. The dotted lines in each graph refer to the mean on non-infected mice, and the individual values are represented in Figure S4. Unpaired Brown-Forsythe and Welch ANOVA tests were used to perform comparisons between groups. Differences between groups were considered significant if $p < 0.05$. *p* values shown above bars refer to differences to non-infected mice.

infections with alpha or delta variants, thus, together with differential chemokine expression, explaining the lung and blood neutrophilia. In contrast, a more balanced BM neutrophil/monocyte output may be occurring in infections with the omicron variant. It will be interesting to pursue these data to unravel the mechanisms dictating BM adaptation to SARS-CoV-2 infection. Inflammatory cytokines, as IFN-γ, IL-1β, IL-6, G-CSF, and GM-CSF, have been described as signals of emergency myelopoiesis during infection.[27,57] Type I IFN has also been incriminated as the driver of emergency myelopoiesis in models of lymphocytic choriomeningitis virus (LCMV) infections.[58] Thus, these molecules are good candidates to operate also during SARS-CoV-2 infections.

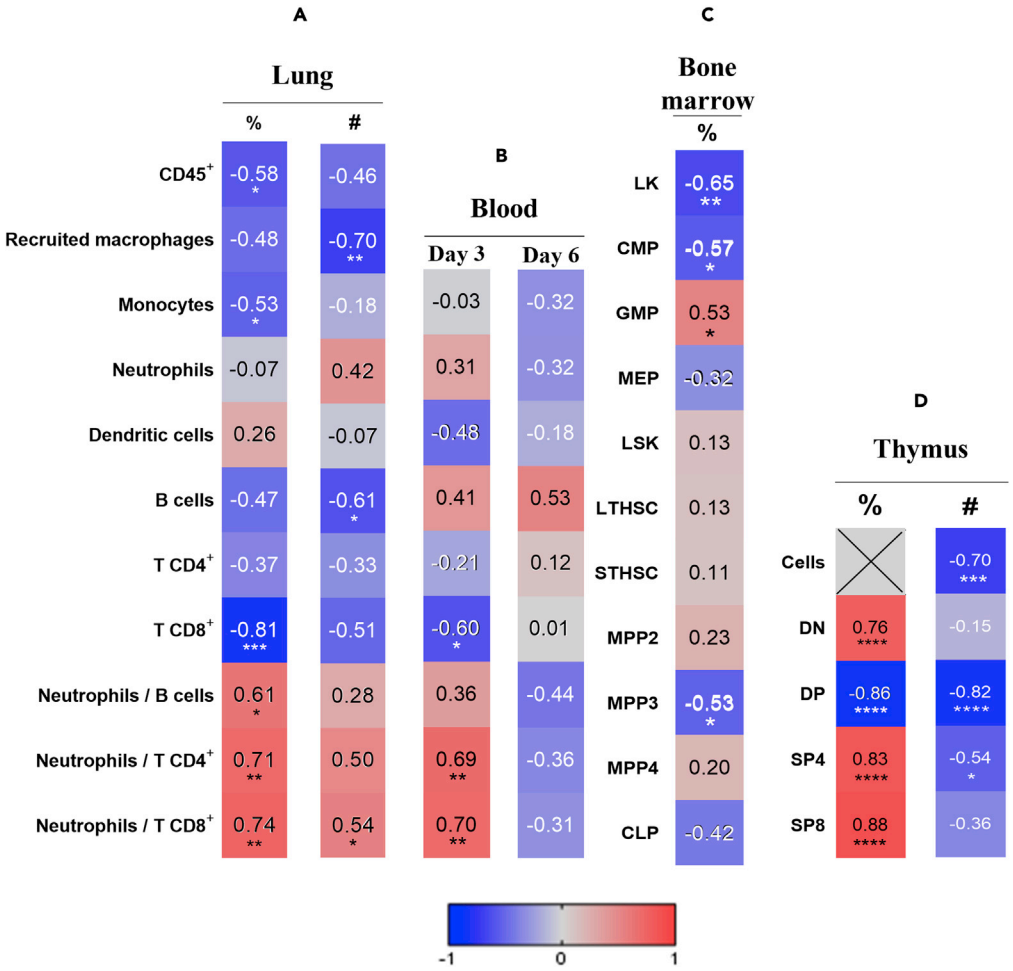

Figure 7. Altered immune responses in the lung, blood and primary lymphoid organs correlate with disease severity

(A–D)Pearson correlations calculated for frequency and number of immune cell populations or ratios obtained in the A. lung, B. blood, C. BM and D. thymus with the clinical score obtained on days 3 or 6 post-infection, for all animals in the three infections. A two-tailed Pearson test was conducted to correlate the clinical score and each cell population. Correlations were defined as weak if $r = 0$ to 0.3; moderate if $r = 0.3$ to 0.5; strong if $r = 0.5$ to 0.7; and very strong if $r = 0.7$ to 1. Differences between groups were considered significant if $p < 0.05$. *p<0.05; **p<0.01; ***p<0.001; ****p<0.0001.

To our knowledge, this is the first report showing that the thymus is a target of SARS-CoV-2 infection. However, there have been hints of thymic involvement in COVID-19 pathogenesis, possibly due to the hyper-inflammatory response observed during infection. A study comparing the thymic-thoracic ratio in 28-36-week-old fetuses reported that COVID-19 infection reduced fetal thymus size in pregnant women with mild or moderate symptoms after recovery from the infection.[59] Another study showed thymic alterations in SARS-CoV-2 infected non-human primates, which included evidence of viral particles in the thymus and increased apoptosis of thymocytes.[60] This study further showed that the administration of Azvudine, a nucleoside analogue that inhibits HIV-1 RNA-dependent RNA polymerase, to non-human primates or humans with COVID-19 had beneficial effects, which in the case of non-human primates associated with thymus recovery.[60] It is tempting to speculate that the impact of the infection in the thymus may underlie important alterations seen at the periphery, namely the reduction in $CD4^+$ and $CD8^+$ cell counts in patients with COVID-19 which closely correlate with disease progression.[61] Also, it has been proposed that the aged thymus may be more susceptible to the virus impact and therefore associate with the increased susceptibility to severe disease reported in the elderly.[62] As the generative site for T cells, the thymus may be a key regulatory organ in the response and recovery of severe SARS-CoV-2-induced diseases. The underlying mechanisms leading to thymic atrophy remain to be elucidated, but several hypotheses are worth

exploring in future studies. Firstly, changes in the thymus may be promoted by alterations in the BM and a reduction in thymic seeding progenitors.[38] Secondly, the systemic cytokine storm promoted by infection may lead to massive death of developing thymocytes.[63] Thirdly, as we detected viral PFUs in the thymi of infected animals, one can consider that the direct infection of the organ may also alter the functionality of the thymic stromal microenvironment,[64] indirectly conditioning T cell generation. Intrathymic and pre-thymic stages of T cell development depend respectively on complex thymic (thymic epithelial cells, mesenchymal cells, endothelial cells) and BM (mesenchymal progenitors, osteoblasts, fibroblasts, adipocytes, and endothelial cells) stromal microenvironments.[65,66] Future studies should aim at evaluating the direct impact of SARS-CoV2 infection on the homeostasis and function of key BM and thymic stromal populations, as alterations in these supportive hematopoietic niches may impact on the hematopoietic process.

The study presented here contributes to a better understanding of the impact of the SARS-CoV-2 variant diversity to the infection course and the characteristics of the immune response, using the k18-hACE2 mouse as a model. We provide evidence for an attenuation of the omicron variant across several organismal, organ, and cellular parameters, which can be used in the future as read-outs when testing COVID-19 interventions in this mouse model. We also show the impact of infection on the BM and thymus, generating hypotheses for other research avenues of translational relevance.

Limitations of the study

The relatively small animal group sizes together with variations in some of the parameters limit the statistical power of the analysis. Still, when comparable, our data are in line with previously reported studies.[14,18,19] Sex and age differences were not accounted for in our study, as all mice used were 8-12 weeks old females. It will be interesting to investigate our findings in the context of these two variables. Most of our read-outs are focused on day 6 post-infection. Previous reports showed that a progressive inflammatory process occurs during the infection of k18-hACE2 mice upon SARS-CoV-2 infection, starting as soon as day 2 post-infection.[11,15,30] Thus, it will be interesting to address some of our findings in a kinetic way, both investigating changes at earlier and later time points post-infection. We anticipate the omicron VOC as the most interesting to pursue these studies in the future.

STAR★METHODS

Detailed methods are provided in the online version of this paper and include the following:

- KEY RESOURCES TABLE
- RESOURCE AVAILABILITY
  - Lead contact
  - Materials availability
  - Data and code availability
- EXPERIMENTAL MODEL AND SUBJECT DETAILS
  - Virus propagation and titration
  - Mice and intranasal infection
- METHOD DETAILS
  - Clinical and organ scores
  - Histology and immunohistochemistry
  - Cytokine detection
  - FACS analysis
  - RNA analysis
- QUANTIFICATION AND STATISTICAL ANALYSIS

SUPPLEMENTAL INFORMATION

Supplemental information can be found online at https://doi.org/10.1016/j.isci.2023.105972.

ACKNOWLEDGMENTS

The following reagents were deposited by the Centers for Disease Control and Prevention and obtained through BEI Resources, NIAID, NIH: SARS-Related Coronavirus 2, Isolate hCoV-19/England/204820464/2020 (alpha variant), NR-54000; SARS-Related Coronavirus 2, Isolate hCoV-19/USA/PHC658/2021 (delta

variant), NR-55611; SARS-Related Coronavirus 2 Isolate hCoV-19/USA/MD-HP20874/2021 (omicron variant), NR-56461.

This work was supported by a BSAC COVID-19 grant to M.S. (#BSAC-COVID-98). We thank Ana Cordeiro Gomes for the assistance with the graphical abstract.

M.S. and N.L.A. are sponsored by FCT through CEEC contracts.

AUTHOR CONTRIBUTIONS

Conceptualization, M.S.; methodology, M.S., S.L., N.L.A., P.F., J.C., and R.G.; investigation, M.S., S.L., A.I.F., M.L.S., D.S., J.M.C., P.F., J.C., and R.G.; formal analysis, M.S., J.C., and R.G.; writing – original draft, M.S.; writing – review & editing, M.S., S.L., N.L.A., P.M., J.C., and R.G.; visualization, M.S., P.F., J.C., and R.G.; funding acquisition, M.S.

DECLARATION OF INTERESTS

The authors declare no competing interests.

INCLUSION AND DIVERSITY

We support inclusive, diverse, and equitable conduct of research.

Received: August 24, 2022
Revised: December 5, 2022
Accepted: January 9, 2023
Published: February 17, 2023

REFERENCES

1. de Souza, A.S., de Freitas Amorim, V.M., Guardia, G.D.A., Dos Santos, F.F., Ulrich, H., Galante, P.A.F., de Souza, R.F., and Guzzo, C.R. (2022). Severe acute respiratory syndrome coronavirus 2 variants of concern: a perspective for emerging more transmissible and vaccine-resistant strains. Viruses *14*. https://doi.org/10.3390/v14040827.

2. Flores-Vega, V.R., Monroy-Molina, J.V., Jimenez-Hernandez, L.E., Torres, A.G., Santos-Preciado, J.I., and Rosales-Reyes, R. (2022). SARS-CoV-2: evolution and emergence of new viral variants. Viruses *14*. https://doi.org/10.3390/v14040653.

3. McLean, G., Kamil, J., Lee, B., Moore, P., Schulz, T.F., Muik, A., Sahin, U., Türeci, Ö., and Pather, S. (2022). The impact of evolving SARS-CoV-2 mutations and variants on COVID-19 vaccines. mBio *13*, e0297921. https://doi.org/10.1128/mbio.02979-21.

4. Muñoz-Fontela, C., Dowling, W.E., Funnell, S.G.P., Gsell, P.S., Riveros-Balta, A.X., Albrecht, R.A., Andersen, H., Baric, R.S., Carroll, M.W., Cavaleri, M., et al. (2020). Animal models for COVID-19. Nature *586*, 509–515. https://doi.org/10.1038/s41586-020-2787-6.

5. Hassan, A.O., Case, J.B., Winkler, E.S., Thackray, L.B., Kafai, N.M., Bailey, A.L., McCune, B.T., Fox, J.M., Chen, R.E., Alsoussi, W.B., et al. (2020). A SARS-CoV-2 infection model in mice demonstrates protection by neutralizing antibodies. Cell *182*, 744–753.e4. https://doi.org/10.1016/j.cell.2020.06.011.

6. Bao, L., Deng, W., Huang, B., Gao, H., Liu, J., Ren, L., Wei, Q., Yu, P., Xu, Y., Qi, F., et al. (2020). The pathogenicity of SARS-CoV-2 in hACE2 transgenic mice. Nature *583*, 830–833. https://doi.org/10.1038/s41586-020-2312-y.

7. Sun, S.H., Chen, Q., Gu, H.J., Yang, G., Wang, Y.X., Huang, X.Y., Liu, S.S., Zhang, N.N., Li, X.F., Xiong, R., et al. (2020). A mouse model of SARS-CoV-2 infection and pathogenesis. Cell Host Microbe *28*, 124–133.e4. https://doi.org/10.1016/j.chom.2020.05.020.

8. McCray, P.B., Jr., Pewe, L., Wohlford-Lenane, C., Hickey, M., Manzel, L., Shi, L., Netland, J., Jia, H.P., Halabi, C., Sigmund, C.D., et al. (2007). Lethal infection of K18-hACE2 mice infected with severe acute respiratory syndrome coronavirus. J. Virol. *81*, 813–821. https://doi.org/10.1128/JVI.02012-06.

9. Dong, W., Mead, H., Tian, L., Park, J.G., Garcia, J.I., Jaramillo, S., Barr, T., Kollath, D.S., Coyne, V.K., Stone, N.E., et al. (2022). The K18-human ACE2 transgenic mouse model recapitulates non-severe and severe COVID-19 in response to an infectious dose of the SARS-CoV-2 virus. J. Virol. *96*, e0096421. https://doi.org/10.1128/JVI.00964-21.

10. Kumari, P., Rothan, H.A., Natekar, J.P., Stone, S., Pathak, H., Strate, P.G., Arora, K., Brinton, M.A., and Kumar, M. (2021). Neuroinvasion and encephalitis following intranasal inoculation of SARS-CoV-2 in K18-hACE2 mice. Viruses *13*. https://doi.org/10.3390/v13010132.

11. Oladunni, F.S., Park, J.G., Pino, P.A., Gonzalez, O., Akhter, A., Allué-Guardia, A., Olmo-Fontánez, A., Gautam, S., Garcia-Vilanova, A., Ye, C., et al. (2020). Lethality of SARS-CoV-2 infection in K18 human angiotensin-converting enzyme 2 transgenic mice. Nat. Commun. *11*, 6122. https://doi.org/10.1038/s41467-020-19891-7.

12. Radvak, P., Kwon, H.J., Kosikova, M., Ortega-Rodriguez, U., Xiang, R., Phue, J.N., Shen, R.F., Rozzelle, J., Kapoor, N., Rabara, T., et al. (2021). SARS-CoV-2 B.1.1.7 (alpha) and B.1.351 (beta) variants induce pathogenic patterns in K18-hACE2 transgenic mice distinct from early strains. Nat. Commun. *12*, 6559. https://doi.org/10.1038/s41467-021-26803-w.

13. Rathnasinghe, R., Strohmeier, S., Amanat, F., Gillespie, V.L., Krammer, F., García-Sastre, A., Coughlan, L., Schotsaert, M., and Uccellini, M.B. (2020). Comparison of transgenic and adenovirus hACE2 mouse models for SARS-CoV-2 infection. Emerg. Microb. Infect. *9*, 2433–2445. https://doi.org/10.1080/22221751.2020.1838955.

14. Stolp, B., Stern, M., Ambiel, I., Hofmann, K., Morath, K., Gallucci, L., Cortese, M., Bartenschlager, R., Ruggieri, A., Graw, F., et al. (2022). SARS-CoV-2 variants of concern display enhanced intrinsic pathogenic properties and expanded organ tropism in mouse models. Cell Rep. *38*, 110387. https://doi.org/10.1016/j.celrep.2022.110387.

15. Zheng, J., Wong, L.Y.R., Li, K., Verma, A.K., Ortiz, M.E., Wohlford-Lenane, C., Leidinger, M.R., Knudson, C.M., Meyerholz, D.K., McCray, P.B., Jr., and Perlman, S. (2021).

COVID-19 treatments and pathogenesis including anosmia in K18-hACE2 mice. Nature *589*, 603–607. https://doi.org/10.1038/s41586-020-2943-z.

16. Guan, W.J., and Zhong, N.S. (2020). Clinical characteristics of covid-19 in China. Reply. N. Engl. J. Med. *382*, 1861–1862. https://doi.org/10.1056/NEJMc2005203.

17. Mao, T., Israelow, B., Lucas, C., Vogels, C.B.F., Gomez-Calvo, M.L., Fedorova, O., Breban, M.I., Menasche, B.L., Dong, H., Linehan, M., et al. (2022). A stem-loop RNA RIG-I agonist protects against acute and chronic SARS-CoV-2 infection in mice. J. Exp. Med. *219*, e20211818. https://doi.org/10.1084/jem.20211818.

18. Halfmann, P.J., Iida, S., Iwatsuki-Horimoto, K., Maemura, T., Kiso, M., Scheaffer, S.M., Darling, T.L., Joshi, A., Loeber, S., Singh, G., et al. (2022). SARS-CoV-2 Omicron virus causes attenuated disease in mice and hamsters. Nature *603*, 687–692. https://doi.org/10.1038/s41586-022-04441-6.

19. Shuai, H., Chan, J.F.W., Hu, B., Chai, Y., Yuen, T.T.T., Yin, F., Huang, X., Yoon, C., Hu, J.C., Liu, H., et al. (2022). Attenuated replication and pathogenicity of SARS-CoV-2 B.1.1.529 Omicron. Nature *603*, 693–699. https://doi.org/10.1038/s41586-022-04442-5.

20. Guo, Y., Han, J., Zhang, Y., He, J., Yu, W., Zhang, X., Wu, J., Zhang, S., Kong, Y., Guo, Y., et al. (2022). SARS-CoV-2 omicron variant: epidemiological features, biological characteristics, and clinical significance. Front. Immunol. *13*, 877101. https://doi.org/10.3389/fimmu.2022.877101.

21. Wolter, N., Jassat, W., Walaza, S., Welch, R., Moultrie, H., Groome, M., Amoako, D.G., Everatt, J., Bhiman, J.N., Scheepers, C., et al. (2022). Early assessment of the clinical severity of the SARS-CoV-2 omicron variant in South Africa: a data linkage study. Lancet *399*, 437–446. https://doi.org/10.1016/S0140-6736(22)00017-4.

22. Zhan, Y., Yin, H., and Yin, J.Y. (2022). B.1.617.2 (Delta) Variant of SARS-CoV-2: features, transmission and potential strategies. Int. J. Biol. Sci. *18*, 1844–1851. https://doi.org/10.7150/ijbs.66881.

23. Cao, X. (2020). COVID-19: immunopathology and its implications for therapy. Nat. Rev. Immunol. *20*, 269–270. https://doi.org/10.1038/s41577-020-0308-3.

24. Schulte-Schrepping, J., Reusch, N., Paclik, D., Baßler, K., Schlickeiser, S., Zhang, B., Krämer, B., Krammer, T., Brumhard, S., Bonaguro, L., et al. (2020). Severe COVID-19 is marked by a dysregulated myeloid cell compartment. Cell *182*, 1419–1440.e23. https://doi.org/10.1016/j.cell.2020.08.001.

25. Shahbaz, S., Xu, L., Osman, M., Sligl, W., Shields, J., Joyce, M., Tyrrell, D.L., Oyegbami, O., and Elahi, S. (2021). Erythroid precursors and progenitors suppress adaptive immunity and get invaded by SARS-CoV-2. Stem Cell Rep. *16*, 1165–1181. https://doi.org/10.1016/j.stemcr.2021.04.001.

26. Mei, H., Luo, L., and Hu, Y. (2020). Thrombocytopenia and thrombosis in hospitalized patients with COVID-19. J. Hematol. Oncol. *13*, 161. https://doi.org/10.1186/s13045-020-01003-z.

27. Gomes, A.C., Saraiva, M., and Gomes, M.S. (2021). The bone marrow hematopoietic niche and its adaptation to infection. Semin. Cell Dev. Biol. *112*, 37–48. https://doi.org/10.1016/j.semcdb.2020.05.014.

28. Cowan, J.E., Takahama, Y., Bhandoola, A., and Ohigashi, I. (2020). Postnatal involution and counter-involution of the thymus. Front. Immunol. *11*, 897. https://doi.org/10.3389/fimmu.2020.00897.

29. Bayarri-Olmos, R., Johnsen, L.B., Idorn, M., Reinert, L.S., Rosbjerg, A., Vang, S., Hansen, C.B., Helgstrand, C., Bjelke, J.R., Bak-Thomsen, T., et al. (2021). The alpha/B.1.1.7 SARS-CoV-2 variant exhibits significantly higher affinity for ACE-2 and requires lower inoculation doses to cause disease in K18-hACE2 mice. Elife *10*, e70002. https://doi.org/10.7554/eLife.70002.

30. Winkler, E.S., Bailey, A.L., Kafai, N.M., Nair, S., McCune, B.T., Yu, J., Fox, J.M., Chen, R.E., Earnest, J.T., Keeler, S.P., et al. (2020). SARS-CoV-2 infection of human ACE2-transgenic mice causes severe lung inflammation and impaired function. Nat. Immunol. *21*, 1327–1335. https://doi.org/10.1038/s41590-020-0778-2.

31. Ullman-Culleré, M.H., and Foltz, C.J. (1999). Body condition scoring: a rapid and accurate method for assessing health status in mice. Lab. Anim. Sci. *49*, 319–323.

32. Yinda, C.K., Port, J.R., Bushmaker, T., Offei Owusu, I., Purushotham, J.N., Avanzato, V.A., Fischer, R.J., Schulz, J.E., Holbrook, M.G., Hebner, M.J., et al. (2021). K18-hACE2 mice develop respiratory disease resembling severe COVID-19. PLoS Pathog. *17*, e1009195. https://doi.org/10.1371/journal.ppat.1009195.

33. Zheng, J., Wang, Y., Li, K., Meyerholz, D.K., Allamargot, C., and Perlman, S. (2021). Severe acute respiratory syndrome coronavirus 2-induced immune activation and death of monocyte-derived human macrophages and dendritic cells. J. Infect. Dis. *223*, 785–795. https://doi.org/10.1093/infdis/jiaa753.

34. Bergamaschi, L., Mescia, F., Turner, L., Hanson, A.L., Kotagiri, P., Dunmore, B.J., Ruffieux, H., De Sa, A., Huhn, O., Morgan, M.D., et al. (2021). Longitudinal analysis reveals that delayed bystander CD8+ T cell activation and early immune pathology distinguish severe COVID-19 from mild disease. Immunity *54*, 1257–1275.e8. https://doi.org/10.1016/j.immuni.2021.05.010.

35. Moss, P. (2022). The T cell immune response against SARS-CoV-2. Nat. Immunol. *23*, 186–193. https://doi.org/10.1038/s41590-021-01122-w.

36. Capucetti, A., Albano, F., and Bonecchi, R. (2020). Multiple roles for chemokines in neutrophil biology. Front. Immunol. *11*, 1259. https://doi.org/10.3389/fimmu.2020.01259.

37. Wilk, A.J., Lee, M.J., Wei, B., Parks, B., Pi, R., Martínez-Colón, G.J., Ranganath, T., Zhao, N.Q., Taylor, S., Becker, W., et al. (2021). Multi-omic profiling reveals widespread dysregulation of innate immunity and hematopoiesis in COVID-19. J. Exp. Med. *218*, e20210582. https://doi.org/10.1084/jem.20210582.

38. Rodrigues, P.M., Ribeiro, A.R., Serafini, N., Meireles, C., Di Santo, J.P., and Alves, N.L. (2018). Intrathymic deletion of IL-7 reveals a contribution of the bone marrow to thymic rebound induced by androgen blockade. J. Immunol. *200*, 1389–1398. https://doi.org/10.4049/jimmunol.1701112.

39. Sigal, A., Milo, R., and Jassat, W. (2022). Estimating disease severity of Omicron and Delta SARS-CoV-2 infections. Nat. Rev. Immunol. *22*, 267–269. https://doi.org/10.1038/s41577-022-00720-5.

40. Ziegler, C.G.K., Allon, S.J., Nyquist, S.K., Mbano, I.M., Miao, V.N., Tzouanas, C.N., Cao, Y., Yousif, A.S., Bals, J., Hauser, B.M., et al. (2020). SARS-CoV-2 receptor ACE2 is an interferon-stimulated gene in human airway epithelial cells and is detected in specific cell subsets across tissues. Cell *181*, 1016–1035.e19. https://doi.org/10.1016/j.cell.2020.04.035.

41. Diorio, C., Henrickson, S.E., Vella, L.A., McNerney, K.O., Chase, J., Burudpakdee, C., Lee, J.H., Jasen, C., Balamuth, F., Barrett, D.M., et al. (2020). Multisystem inflammatory syndrome in children and COVID-19 are distinct presentations of SARS-CoV-2. J. Clin. Invest. *130*, 5967–5975. https://doi.org/10.1172/JCI140970.

42. Gustine, J.N., and Jones, D. (2021). Immunopathology of hyperinflammation in COVID-19. Am. J. Pathol. *191*, 4–17. https://doi.org/10.1016/j.ajpath.2020.08.009.

43. Laing, A.G., Lorenc, A., Del Molino Del Barrio, I., Das, A., Fish, M., Monin, L., Muñoz-Ruiz, M., McKenzie, D.R., Hayday, T.S., Francos-Quijorna, I., et al. (2020). A dynamic COVID-19 immune signature includes associations with poor prognosis. Nat. Med. *26*, 1623–1635. https://doi.org/10.1038/s41591-020-1038-6.

44. Junqueira, C., Crespo, Â., Ranjbar, S., de Lacerda, L.B., Lewandrowski, M., Ingber, J., Parry, B., Ravid, S., Clark, S., Schrimpf, M.R., et al. (2022). FcgammaR-mediated SARS-CoV-2 infection of monocytes activates inflammation. Nature *606*, 576–584. https://doi.org/10.1038/s41586-022-04702-4.

45. Sefik, E., Qu, R., Junqueira, C., Kaffe, E., Mirza, H., Zhao, J., Brewer, J.R., Han, A., Steach, H.R., Israelow, B., et al. (2022). Inflammasome activation in infected macrophages drives COVID-19 pathology. Nature *606*, 585–593. https://doi.org/10.1038/s41586-022-04802-1.

46. Ferreira, A.C., Soares, V.C., de Azevedo-Quintanilha, I.G., Dias, S.d.S.G., Fintelman-Rodrigues, N., Sacramento, C.Q., Mattos, M., de Freitas, C.S., Temerozo, J.R., Teixeira, L., et al. (2021). SARS-CoV-2 engages inflammasome and pyroptosis in human

primary monocytes. Cell Death Dis. *7*, 43. https://doi.org/10.1038/s41420-021-00428-w.

47. Pontelli, M.C., Castro, Í.A., Martins, R.B., La Serra, L., Veras, F.P., Nascimento, D.C., Silva, C.M., Cardoso, R.S., Rosales, R., Gomes, R., et al. (2022). SARS-CoV-2 productively infects primary human immune system cells in vitro and in COVID-19 patients. J. Mol. Cell Biol. *14*, mjac021. https://doi.org/10.1093/jmcb/mjac021.

48. Hui, K.P.Y., Cheung, M.C., Perera, R.A.P.M., Ng, K.C., Bui, C.H.T., Ho, J.C.W., Ng, M.M.T., Kuok, D.I.T., Shih, K.C., Tsao, S.W., et al. (2020). Tropism, replication competence, and innate immune responses of the coronavirus SARS-CoV-2 in human respiratory tract and conjunctiva: an analysis in ex-vivo and in-vitro cultures. Lancet Respir. Med. *8*, 687–695. https://doi.org/10.1016/S2213-2600(20)30193-4.

49. Shen, X.R., Geng, R., Li, Q., Chen, Y., Li, S.F., Wang, Q., Min, J., Yang, Y., Li, B., Jiang, R.D., et al. (2022). ACE2-independent infection of T lymphocytes by SARS-CoV-2. Signal Transduct. Targeted Ther. *7*, 83. https://doi.org/10.1038/s41392-022-00919-x.

50. Helms, J., Kremer, S., Merdji, H., Clere-Jehl, R., Schenck, M., Kummerlen, C., Collange, O., Boulay, C., Fafi-Kremer, S., Ohana, M., et al. (2020). Neurologic features in severe SARS-CoV-2 infection. N. Engl. J. Med. *382*, 2268–2270. https://doi.org/10.1056/NEJMc2008597.

51. Lai, C.C., Ko, W.C., Lee, P.I., Jean, S.S., and Hsueh, P.R. (2020). Extra-respiratory manifestations of COVID-19. Int. J. Antimicrob. Agents *56*, 106024. https://doi.org/10.1016/j.ijantimicag.2020.106024.

52. Xydakis, M.S., Dehgani-Mobaraki, P., Holbrook, E.H., Geisthoff, U.W., Bauer, C., Hautefort, C., Herman, P., Manley, G.T., Lyon, D.M., and Hopkins, C. (2020). Smell and taste dysfunction in patients with COVID-19. Lancet Infect. Dis. *20*, 1015–1016. https://doi.org/10.1016/S1473-3099(20)30293-0.

53. Fumagalli, V., Ravà, M., Marotta, D., Di Lucia, P., Laura, C., Sala, E., Grillo, M., Bono, E., Giustini, L., Perucchini, C., et al. (2022). Administration of aerosolized SARS-CoV-2 to K18-hACE2 mice uncouples respiratory infection from fatal neuroinvasion. Sci. Immunol. *7*, eabl9929. https://doi.org/10.1126/sciimmunol.abl9929.

54. Kaneko, N., Kuo, H.H., Boucau, J., Farmer, J.R., Allard-Chamard, H., Mahajan, V.S., Piechocka-Trocha, A., Lefteri, K., Osborn, M., Bals, J., et al. (2020). Loss of bcl-6-expressing T follicular helper cells and germinal Centers in COVID-19. Cell *183*, 143–157.e13. https://doi.org/10.1016/j.cell.2020.08.025.

55. Trevelin, S.C., Pickering, S., Todd, K., Bishop, C., Pitcher, M., Garrido Mesa, J., Montorsi, L., Spada, F., Petrov, N., Green, A., et al. (2022). Disrupted peyer's patch microanatomy in COVID-19 including germinal centre atrophy independent of local virus. Front. Immunol. *13*, 838328. https://doi.org/10.3389/fimmu.2022.838328.

56. Wilk, A.J., Rustagi, A., Zhao, N.Q., Roque, J., Martínez-Colón, G.J., McKechnie, J.L., Ivison, G.T., Ranganath, T., Vergara, R., Hollis, T., et al. (2020). A single-cell atlas of the peripheral immune response in patients with severe COVID-19. Nat. Med. *26*, 1070–1076. https://doi.org/10.1038/s41591-020-0944-y.

57. Boettcher, S., and Manz, M.G. (2017). Regulation of inflammation- and infection-driven hematopoiesis. Trends Immunol. *38*, 345–357. https://doi.org/10.1016/j.it.2017.01.004.

58. Binder, D., Fehr, J., Hengartner, H., and Zinkernagel, R.M. (1997). Virus-induced transient bone marrow aplasia: major role of interferon-alpha/beta during acute infection with the noncytopathic lymphocytic choriomeningitis virus. J. Exp. Med. *185*, 517–530. https://doi.org/10.1084/jem.185.3.517.

59. Goncu Ayhan, S., Turgut, E., Oluklu, D., Ozden Tokalioglu, E., Menekse Beser, D., Moraloglu Tekin, O., and Sahin, D. (2022). Influence of Covid-19 infection on fetal thymus size after recovery. J. Perinat. Med. *50*, 139–143. https://doi.org/10.1515/jpm-2021-0322.

60. Zhang, J.L., Li, Y.H., Wang, L.L., Liu, H.Q., Lu, S.Y., Liu, Y., Li, K., Liu, B., Li, S.Y., Shao, F.M., et al. (2021). Azvudine is a thymus-homing anti-SARS-CoV-2 drug effective in treating COVID-19 patients. Signal Transduct. Targeted Ther. *6*, 414. https://doi.org/10.1038/s41392-021-00835-6.

61. Zhang, X., Tan, Y., Ling, Y., Lu, G., Liu, F., Yi, Z., Jia, X., Wu, M., Shi, B., Xu, S., et al. (2020). Viral and host factors related to the clinical outcome of COVID-19. Nature *583*, 437–440. https://doi.org/10.1038/s41586-020-2355-0.

62. Wang, W., Thomas, R., Oh, J., and Su, D.M. (2021). Thymic aging may Be associated with COVID-19 pathophysiology in the elderly. Cells *10*. https://doi.org/10.3390/cells10030628.

63. Borges, M., Barreira-Silva, P., Flórido, M., Jordan, M.B., Correia-Neves, M., and Appelberg, R. (2012). Molecular and cellular mechanisms of Mycobacterium avium-induced thymic atrophy. J. Immunol. *189*, 3600–3608. https://doi.org/10.4049/jimmunol.1201525.

64. Holländer, G.A., Krenger, W., and Blazar, B.R. (2010). Emerging strategies to boost thymic function. Curr. Opin. Pharmacol. *10*, 443–453. https://doi.org/10.1016/j.coph.2010.04.008.

65. Crane, G.M., Jeffery, E., and Morrison, S.J. (2017). Adult haematopoietic stem cell niches. Nat. Rev. Immunol. *17*, 573–590. https://doi.org/10.1038/nri.2017.53.

66. Han, J., and Zúñiga-Pflücker, J.C. (2021). A 2020 view of thymus stromal cells in T cell development. J. Immunol. *206*, 249–256. https://doi.org/10.4049/jimmunol.2000889.

67. Berg, S., Kutra, D., Kroeger, T., Straehle, C.N., Kausler, B.X., Haubold, C., Schiegg, M., Ales, J., Beier, T., Rudy, M., et al. (2019). Ilastik: interactive machine learning for (bio) image analysis. Nat. Methods *16*, 1226–1232.

68. Lamprecht, M.R., Sabatini, D.M., and Carpenter, A.E. (2007). CellProfiler: free, versatile software for automated biological image analysis. Biotechniques *42*, 71–75. PMID: 17269487.

69. Baer, A., and Kehn-Hall, K. (2014). Viral concentration determination through plaque assays: using traditional and novel overlay systems. JoVE *4*, e52065. https://doi.org/10.3791/52065.

70. Klein, S., Cortese, M., Winter, S.L., Wachsmuth-Melm, M., Neufeldt, C.J., Cerikan, B., Stanifer, M.L., Boulant, S., Bartenschlager, R., and Chlanda, P. (2020). SARS-CoV-2 structure and replication characterized by in situ cryo-electron tomography. Nat. Commun. *11*, 5885. https://doi.org/10.1038/s41467-020-19619-7.

71. Fonseca, K.L., Maceiras, A.R., Matos, R., Simoes-Costa, L., Sousa, J., Ca, B., Barros, L., Fernandes, A.I., Mereiter, S., Reis, R., et al. (2020). Deficiency in the glycosyltransferase Gcnt1 increases susceptibility to tuberculosis through a mechanism involving neutrophils. Mucosal Immunol. *13*, 836–848. https://doi.org/10.1038/s41385-020-0277-7.

72. Cardoso, A., Martins, A.C., Maceiras, A.R., Liu, W., Castro, I., Castro, A.G., Bandeira, A., Di Santo, J.P., Cumano, A., Li, Y., et al. (2021). Interleukin-10 induces interferon-gamma-dependent emergency myelopoiesis. Cell Rep. *37*, 109887. https://doi.org/10.1016/j.celrep.2021.109887.

73. An, D., Li, K., Rowe, D.K., Diaz, M.C.H., Griffin, E.F., Beavis, A.C., Johnson, S.K., Padykula, I., Jones, C.A., Briggs, K., et al. (2021). Protection of K18-hACE2 mice and ferrets against SARS-CoV-2 challenge by a single-dose mucosal immunization with a parainfluenza virus 5-based COVID-19 vaccine. Sci. Adv. *7*, eabi5246. https://doi.org/10.1126/sciadv.abi5246.

74. Vandesompele, J., De Preter, K., Pattyn, F., Poppe, B., Van Roy, N., De Paepe, A., and Speleman, F. (2002). Accurate normalization of real-time quantitative RT-PCR data by geometric averaging of multiple internal control genes. Genome Biol. *3*. RESEARCH0034. https://doi.org/10.1186/gb-2002-3-7-research0034.

75. Pfaffl, M.W. (2001). A new mathematical model for relative quantification in real-time RT-PCR. Nucleic Acids Res. *29*, e45. https://doi.org/10.1093/nar/29.9.e45.

STAR★METHODS

KEY RESOURCES TABLE

REAGENT or RESOURCE	SOURCE	IDENTIFIER
Antibodies		
PE anti-mouse CD45	Biolegend	Cat#103106 (30-F11, 1:400); RRID:AB_312971
Brilliant Violet 785™ anti-mouse CD4	Biolegend	Cat#100453 (GK1.5, 1:200); RRID:AB_2565843
APC/Cyanine7 anti-mouse CD19	Biolegend	Cat#115530 (6D5, 1:100); RRID:AB_830707
Brilliant Violet 510™ anti-mouse/human CD11b	Biolegend	Cat#101245 (M1/70, 1:100); RRID:AB_2561390
PE/Cyanine7 anti-mouse CD11c	Biolegend	Cat#117318 (N418, 1:200); RRID:AB_493568
PerCP/Cyanine5.5 anti-mouse Ly-6G	Biolegend	Cat#127616 (1A8, 1:400); RRID:AB_1877271
Pacific Blue™ anti-mouse Ly-6C	Biolegend	Cat#128014 (HK1.4, 1:400); RRID:AB_1732079
APC anti-mouse CD170 (Siglec-F)	Biolegend	Cat#155508 (S17007L, 1:200); RRID:AB_2750237
Brilliant Violet 650™ anti-mouse CD8a	Biolegend	Cat#100741 (53-6.7, 1:200); RRID:AB_11124344
Zombie Green™ Fixable Viability Kit	Biolegend	Cat#423112 (-, 1:500); RRID:AB_2927787
FITC anti-mouse CD8a	Biolegend	Cat#100804 (5H10-1; 1:200); RRID:AB_312765
TCR gamma/delta Monoclonal Antibody, APC	eBioscience	Cat#17-5711-82 (eBioGL3, 1:400); RRID:AB_842756
Brilliant Violet 421™ anti-mouse CD24	Biolegend	Cat#101825 (M1/69, 1:400); RRID:AB_10901159
Brilliant Violet 605™ anti-mouse CD62L	Biolegend	Cat#104437 (MEL-14, 1:600); RRID:AB_11125577
Brilliant Violet 785™ anti-mouse CD4	Biolegend	Cat#100453 (GK1.5; 1:200); RRID:AB_2565843
PE/Cyanine7 anti-mouse CD69	Biolegend	Cat#104511 (H1.2F3, 1:400); RRID:AB_493565
Zombie Aqua™ Fixable Viability Kit	Biolegend	Cat#423101 (-, 1:500); RRID:AB_2927788
Biotin anti-mouse CD3ε	Biolegend	Cat#100304 (145-2C11, 1:50); RRID:AB_312669
Biotin anti-mouse CD4	Biolegend	Cat#100404 (GK1.5, 1:50); RRID:AB_312689
Biotin anti-mouse CD8a	Biolegend	Cat#100704 (53-6.7, 1:50); RRID:AB_312743
Biotin anti-mouse CD11c	Biolegend	Cat#117304 (N418, 1:50); RRID:AB_313773
Biotin anti-mouse/human CD11b	Biolegend	Cat#101203 (M1/70, 1:50); RRID:AB_312786
Biotin anti-mouse Ly-6G/Ly-6C (Gr-1)	Biolegend	Cat#108404 (RB6-8C5, 1:50); RRID:AB_313369
Biotin anti-mouse CD19	Biolegend	Cat#115504 (6D5, 1:50); RRID:AB_313639
Biotin anti-mouse/human CD45R/B220	Biolegend	Cat#103204 (RA3-6B2, 1:50); RRID:AB_312989
Biotin anti-mouse NK-1.1	Biolegend	Cat#108704 (PK136, 1:50); RRID:AB_313391
Biotin anti-mouse TER-119/Erythroid Cells	Biolegend	Cat#116204 (TER-119, 1:50); RRID:AB_313705
BD Pharmingen™ FITC Rat Anti-Mouse Ly-6A/E, Sca1	BD Biosciences	Cat#553335 (E13-161.7, 1:400); RRID:AB_394791
BD Pharmingen™ PerCP-Cy™5.5 Rat Anti-Mouse CD16/CD32, FcγRIII/FcγRII	BD Biosciences	Cat#560540 (2.4G2, 1:300); RRID:AB_1645259
PE anti-mouse CD135, Flt3	Biolegend	Cat#135305 (A2F10, 1:100); RRID:AB_1877217
PE/Cyanine7 anti-mouse CD127 (IL-7Rα)	Biolegend	Cat#135014 (A7R34, 1:100); RRID:AB_1937265
APC anti-mouse CD48	Biolegend	Cat#103412 (HM48-1, 1:400); RRID:AB_571997
APC/Cyanine7 anti-mouse CD117 (c-kit)	Biolegend	Cat#105825 (2B8, 1:800); RRID:AB_1626280
CD34 Monoclonal Antibody (RAM34), eFluor™ 450	eBioscience	Cat#48-0341-80 (RAM34, 1:50); RRID:AB_2043838
Brilliant Violet 711™ anti-mouse CD150 (SLAM)	Biolegend	Cat#115941 (TC15-12F12.2, 1:200); RRID:AB_2629660
Brilliant Violet 785™ Streptavidin	Biolegend	Cat#405249 (-, 1:200); RRID:AB_2927789
TCR beta Monoclonal Antibody (H57-597), PerCP-Cyanine5.5	Biolegend	Cat#45-5961-80 (H57-597, 1:600); RRID:AB_925764
anti-SARS-CoV-2 nucleocapsid protein rabbit IgG monoclonal antibody	GeneTex	Cat#GTX635679 (1:1000); RRID:AB_2888553
peroxidase AffiniPure Goat Anti-Rabbit IgG (H+L)	Jackson ImmunoResearch	Cat#111-035-144 (1:500); RRID:AB_2307391

(*Continued on next page*)

Continued

REAGENT or RESOURCE	SOURCE	IDENTIFIER
Bacterial and virus strains		
SARS-CoV-2 alpha variant (B.1.1.7)	BEI Resources	NR-55461
SARS-CoV-2 delta variant (B.1.617.2)	BEI Resources	NR-55611
SARS-CoV-2 omicron variant (B.1.1.529.18)	BEI Resources	NR-56461
Critical commercial assays		
TripleXtractor	GRiSP Research Solutions	GB23.0200
ProtoScript First Strand cDNA Synthesis kit	New England Biolabs	E6300L
iTaq Universal SYBR Green Supermix	Bio-Rad	1725120
IFN gamma Mouse Uncoated ELISA Kit with Plates	Invitrogen	88-7314-22
Experimental models: Organisms/strains		
k18-hACE2	Jackson Laboratory	IMSR_JAX:034860
Oligonucleotides		
	See Table S1 for oligonucleotide sequence and reference	
Software and algorithms		
Interactive Learning and Segmentation Toolkit (Ilastik version 1.3.3)	Berg et al.[67]	
CellProfiler Analyst software (version 3.1.5)	Lamprecht et al.[68]	
Prism	Graphpad	
FlowJo	FlowJo, LLC	

RESOURCE AVAILABILITY

Lead contact

Further information and requests for resources and reagents should be directed to and will be fulfilled by the lead contact, Margarida Saraiva (margarida.saraiva@ibmc.up.pt).

Materials availability

This study did not generate new unique reagents.

Data and code availability

Data reported in this paper will be shared by the lead contact upon request. This paper does not report original code. Any additional information required to reanalyze the data reported in this paper is available from the lead contact upon request.

EXPERIMENTAL MODEL AND SUBJECT DETAILS

Virus propagation and titration

All experiments with SARS-CoV-2 were performed under biosafety level 3 containment. The three SARS-CoV-2 variants (alpha, B.1.1.7; delta, B.1.617.2; and omicron, BA.1.18/B.1.1.529.1.18) were obtained from BEI Resources and propagated in VeroE6 cells upon infection with a multiplicity of infection (MOI) of 0.01 for 3–4 days. The infected cultures were monitored every day and the virus containing supernatant harvested when extensive cell damage was observed. Viral stocks were aliquoted, stored at −80°C, and titrated by plaque forming unite (PFU) assay based on previously published protocols.[69,70]

Mice and intranasal infection

Animal experiments were approved by the i3S Animal Ethics Committee and Portuguese Competent Authority (DGAV) and performed at the i3S Animal Facility in accordance with the European Union Directive

2010/63/EU and Portuguese Legislation. The i3S animal facility is AAALAC accredited and follows the Guide for the Care and Use of Laboratory Animals, principle of the Three R's, to replace, reduce, and refine animal use for scientific purposes, as well as FELASA recommendations.

k18-hACE2 female transgenic mice were obtained from Charles River and all animal experiments involving infection were conducted in the certified Animal Biosafety Level 3 (ABSL3) at i3s. Mice were maintained on a 12:12 light cycle at 45–65% humidity and provided *ad libitum* water and standardized synthetic diet (Envigo Teklad Global Rodent Diet, 2014S). For infection, mice were anaesthetized with 2–3% isoflurane and intranasally inoculated with 1×10^4, 5×10^4 or 1×10^5 PFU of the indicated SARS-CoV-2 variant in infection media (DMEM high glucose supplemented with 1% of Penicillin Streptomycin). The intranasal administrations were performed in both nostrils. Naïve k18-hACE2 mice were used as a control group. On day 6 post-infection, mice were euthanized by an intraperitoneal injection of sodium pentobarbital (400mg/kg) and perfused transcardially with PBS. The bronchoalveolar lavage was recovered through canulation of the trachea and collection of liquid in sterile PBS +1% FBS.

METHOD DETAILS

Clinical and organ scores

All animals were enrolled in a 6-day study, being monitored and weighed daily to assess their clinical score (Table 1). Scores were based on general clinical signs, such as weight variation, body condition and activity level, and specific signs of respiratory (dyspnoea) and neurological (ataxia) involvement. Mice were humanely euthanized when reaching the "humane-end-point" (HEP). A clinical score of 15 was considered for the implementation of a HEP of euthanasia as it reflected a significant impairment of the animal general health status and was indicative of an irreversible severe disease outcome. A weight loss higher than 25%, seizures and severe dyspnoea were established HEP, as was unresponsiveness to stimulus for 3 sequential observations (see Table 1 for details), independently of the total score obtained. Four score intervals were considered for decision orientation, as follows: i) 0–5 – minor changes – re-evaluate animal the next day. ii) 6–10 – moderate changes – seek veterinary opinion; re-evaluate after 4 hours; if persistent after 2 followed evaluations, consider hydration and food support or HEP application if one of the scores corresponds to a 3 at behavioural changes (unresponsive to stimulus). iii) 11–14 – major changes – seek veterinary opinion; re-evaluate the animal at a 1 hour interval for a maximum of 3 observations; consider hydration, food support and temperature control; if unchanged apply a HEP. iv) > 15 – critical changes – apply HEP at a maximum period of 1 hour. At HEP or on day 6 post-infection, different organs were collected and a macroscopic scoring assigned based on visible alterations (Table 2 and Figure S2A). Any fat surrounding the collected organ was removed before proceeding with the experimental procedure.

Histology and immunohistochemistry

The lung (right upper lobe), brain (right hemisphere) and nasal turbinates were collected and placed in 10% formalin for >72 hrs. Fixed tissues were embedded in paraffin and tissue sections (3 μm) were processed for histology and immunohistochemistry (IHC). For histologic examination, slides were stained with hematoxylin & eosin (H&E). Scoring of lung histopathological features was based on[18,19] and detailed in Table 3. Quantitative morphometric analysis of lung pathology (% Lesion) was performed using two softwares: Interactive Learning and Segmentation Toolkit (Ilastik version 1.3.3) and CellProfiler Analyst software (version 3.1.5). Probability maps for the lesion area and whole lung are created in Ilastik and analysed in the CellProfiler Analyst software.[71] For viral detection, an IHC assay was performed using an anti-SARS-CoV-2 nucleocapsid protein rabbit IgG monoclonal antibody (GeneTex; GTX635679) at 1:1000 dilution and a peroxidase AffiniPure Goat Anti-Rabbit IgG (H+L) (Jackson ImmunoResearch, 111-035-144) at 1:500 dilution. Images were acquired with a NanoZoomer 2.0- HT Whole Slide Imager, Digital Pathology Slide Scanner.

Cytokine detection

IFN-γ levels were measured in the bronchoalveolar lavage by immunoassay using the Mouse IFNγ quantitative enzyme linked immunosorbent assays (ELISA) kit (Invitrogen; 88-7314-76) and following the manufacturer instructions.

FACS analysis

Blood samples were collected from tail or submandibular veins on days 3 and 6 post-infection, stained with specific conjugated antibodies prior to erythrocyte lysis and fixation with 10 % PFA. Lung cell suspensions

were obtained from half of the remaining four lung lobes upon digestion with Collagenase D. Thymus were recovered from non-infected and infected animals and fat removed. Thymus cell suspensions were prepared by direct organ homogenization and BM suspensions obtained by flushing femurs and tibia. Lung and thymus cell suspensions were directly stained with the indicated antibodies. BM progenitor analysis was performed, involving the depletion of lineage positive cells prior to progenitor cell population staining.[72] All cell suspensions were fixed before data acquisition in a LSRFortessa cytometer (BD Biosciences) using the DIVA 8 software. Analysis after acquisition was performed using FlowJo version 10 (Tree Star Inc). Gating strategies are provided in Figures S3 and S4.

RNA analysis

Total RNA was extracted from 1 × 10^6 lung cells with the TripleXtractor (GRiSP Research Solutions), according to the manufacturer's instructions. RNA quantity was determined using the NanoDrop™ One Spectrophotometer (Thermo Scientific™) and concentrations of 500ng/μL were used for cDNA synthesis. For virus quantification or gene expression, ProtoScript First Strand cDNA Synthesis kit (Biolabs) was used with oligo-dT or random primer mixes, respectively, in a T100 Thermal Cycler (Bio-Rad). qPCR assays were performed using a CFX Connect™ Real-Time PCR Detection System (Bio-Rad). Negative controls and standard curves (constructed with five-fold serial dilutions) were included in each reaction to validate reaction specificity, determine the PCR efficiency and allow virus quantification. For virus quantification, PFU-per-milliliter concentration of each sample was determined based on the original PFU-per-milliliter concentration of the viral stock used for the RNA standard curve.[73] For gene expression, the average expression stability (M-value) of the reference genes and gene relative quantification were assessed based in the geNorm algorithm[74] and the Pfaff method,[75] respectively, included in the CFX Manager™ Software (Bio-Rad). The sequences of the used oligonucleotides are provided in Table S1.

QUANTIFICATION AND STATISTICAL ANALYSIS

Data were analyzed using GraphPad Prism version 8.0 (GraphPad, San Diego, CA, USA). Every dataset was tested for statistical normality and homogeneity of variances, and based on this information, an appropriate statistical test (parametric or nonparametric) was used for multiple comparisons and correlations. Shapiro-Wilk or D'Agostino-Pearson tests were used for analysing normality depending on the sample size, while the unpaired ordinary ANOVA F test was used to test the homogeneity of variances in each group. Each comparison and correlation test used are stated in the respective figure legend. Significant values ($p \leq 0.05$) are indicated in the figures.